

A Pluto–Charon Concerto II. Formation of a Circumbinary Disk of Debris After the Giant Impact

SCOTT J. KENYON

Smithsonian Astrophysical Observatory, 60 Garden Street, Cambridge, MA 02138

BENJAMIN C. BROMLEY

Department of Physics & Astronomy, University of Utah, 201 JFB, Salt Lake City, UT 84112

ABSTRACT

Using a suite of numerical calculations, we consider the long-term evolution of circumbinary debris from the Pluto–Charon giant impact. Initially, these solids have large eccentricity and pericenters near Charon’s orbit. On time scales of 100–1000 yr, dynamical interactions with Pluto and Charon lead to the ejection of most solids from the system. As the dynamics moves particles away from the barycenter, collisional damping reduces the orbital eccentricity of many particles. These solids populate a circumbinary disk in the Pluto–Charon orbital plane; a large fraction of this material lies within a ‘satellite zone’ that encompasses the orbits of Styx, Nix, Kerberos, and Hydra. Compared to the narrow rings generated from the debris of a collision between a trans-Neptunian object (TNO) and Charon (Bromley & Kenyon 2020), disks produced after the giant impact are much more extended and may be a less promising option for producing small circumbinary satellites.

Keywords: planets and satellites: dynamical evolution — planets and satellites: formation — dwarf planets: Pluto

1. INTRODUCTION

For nearly a century, the Pluto–Charon system has provided a new window into the physical processes that shape planetary systems. As the harbinger of the Kuiper belt, the discovery of Pluto contributed a first glimpse of the architecture of the trans-Neptunian region. Combined with light curve data (Andersson & Fix 1973), the identification of Charon on high quality images revealed a tidally-locked binary planet with a short orbital period (6.4 d, Christy & Harrington 1978). Mutual eclipses later enabled novel extraction techniques for the characterization of surface properties and their evolution with time (e.g., Buie et al. 2010a,b). The discovery of four circumbinary satellites – Styx, Nix, Kerberos, and Hydra – yielded new insights into circumbinary orbital dynamics and tidal evolution (Showalter et al. 2011, 2012; Cheng et al. 2014b; Brozović et al. 2015; Showalter & Hamilton 2015). Finally, the spectacular results of the *New Horizons* mission illustrated complex geological processes on frozen worlds and made new connections between surface phenomena on Pluto–Charon and the physical properties of objects in the Kuiper belt (e.g.,

Stern et al. 2015; Grundy et al. 2016; McKinnon et al. 2016; Weaver et al. 2016; Stern et al. 2018; Singer et al. 2019; McKinnon et al. 2020; Singer et al. 2021).

Together with the Earth–Moon system, Pluto–Charon establishes interesting constraints on the frequency of ‘giant impacts’, collisions between massive protoplanets often considered as a final stage of planet formation (e.g., Agnor et al. 1999; Canup & Asphaug 2001; Canup 2004; Agnor & Asphaug 2004; Kenyon & Bromley 2006; Asphaug 2014). In the current picture, mutual gravitational perturbations place growing protoplanets on crossing orbits (see also Wetherill 1980; Lissauer 1987; Weidenschilling et al. 1997; Goldreich et al. 2004). As protoplanet orbits become chaotic, collision velocities become large enough to enable catastrophic collisions, which may lead to complete mergers or binary planets, with additional ejection of debris (e.g., Canup 2005; Asphaug et al. 2006; Canup 2011; Genda et al. 2012; Stewart & Leinhardt 2012; Genda et al. 2015b,a; Kenyon & Bromley 2016; Quintana et al. 2016).

Although many studies elucidate the physical state of material following the Moon-forming impact (e.g., Nakajima & Stevenson 2014; Pahlevan et al. 2016; Lock et al. 2018; Nakajima & Stevenson 2018; Tang & Young 2020), there are few investigations of the evolution of circumbinary debris following the Pluto–Charon collision. Several analyses explain how small satellites on circumbinary orbits become unstable as the central binary expands from a period of 1–2 d to the current 6.4 d (e.g., Ward & Canup 2006; Lithwick & Wu 2008; Youdin et al. 2012; Cheng et al. 2014b; Bromley & Kenyon 2015b; Woo & Lee 2018). Kenyon & Bromley (2014b) and Walsh & Levison (2015) consider how collisional damping converts eccentric circumbinary orbits into the more circular orbits required for the growth of solids into 5–20 km satellites. Bromley & Kenyon (2015b) demonstrate how a swarm of cm-sized pebbles could stabilize satellite orbits throughout the tidal evolution of the central binary.

Here, we examine the evolution of solids orbiting a highly eccentric Pluto–Charon binary. Within the Canup (2005, 2011) smooth particle hydrodynamics (SPH) calculations, there is a broad range of plausible outcomes for the semimajor axis, $a \approx 5\text{--}30 R_P$ (where R_P is the radius of Pluto) and eccentricity, $e \approx 0.1\text{--}0.9$, of the binary planet. The plausible amount of debris surrounding the binary is large, ranging from $\sim 10^{20}$ g up to $\sim 3 \times 10^{23}$ g. The more likely configurations have a mass in debris that is $\sim 10\text{--}1000$ times the total mass of the circumbinary satellites (Kenyon & Bromley 2019a,b). The goal of the present study is to investigate the evolution of solids around very eccentric binaries and to learn whether likely end states of the solids in these systems have the properties needed to explain the current configuration of the circumbinary satellites in the Pluto–Charon system.

The results of this study demonstrate that almost any outcome of a giant impact leads to the production of a stable disk of circumbinary solids. As the central binary tries to eject circumbinary material close to Charon’s orbit, collisions among the solids rapidly damp eccentric orbits. Among a suite of 70 calculations, the amount of solid material in a vertically thin disk depends on the properties of the central binary and the initial mass and orbital properties of the solids. Wider binaries ($a = 10 R_P$, $e = 0.6\text{--}0.8$) retain a larger fraction of the impact debris than more compact binaries ($a = 5 R_P$, $e = 0.2\text{--}0.4$). Circumbinary systems of solids with less mass (10^{21} g) preserve more of their initial mass than more massive swarms with $\sim 10^{23}$ g. All of the 70 calculations maintain enough mass to form several 5–20 km satellites.

After establishing the numerical methods for our calculations in §2, we describe several simulations in detail and summarize global results in §3. We conclude with a discussion (§4) and a brief summary (§5).

2. NUMERICAL METHODS

2.1. Basic Parameters

To set the stage for the calculations, we adopt measured properties of the Pluto–Charon system (Stern et al. 2015; Nimmo et al. 2017; Stern et al. 2018). For an adopted gravitational constant $G = 6.67408 \times 10^{-8}$, Pluto has mass $m_P = 1.303 \times 10^{25}$ g, radius $R_P = 1188.3$ km, and mean density $\rho_P = 1.854$ g cm $^{-3}$. Charon has mass $m_C = 1.586 \times 10^{24}$ g, radius $R_C = 606$ km, and mean density $\rho_C = 1.702$ g cm $^{-3}$. Combined with analyses of HST observations (Brozović et al. 2015; Showalter & Hamilton 2015), detailed n -body calculations (Kenyon & Bromley 2019b) provide limits on the mass of Nix ($m_N \lesssim 4.5 \times 10^{19}$ g) and Hydra ($m_H \lesssim 4.8 \times 10^{19}$ g; see also Youdin, Kratter & Kenyon 2012). Although constraints on the masses of Styx (m_S) and Kerberos (m_K) are more elusive, plausible estimates are $m_S \approx 6 \times 10^{17}$ g and $m_K \approx 10^{18}$ g. Thus, the total mass in satellites is $m_{sat} \approx 10^{20}$ g. These satellites orbit within a ‘satellite zone,’ $a \approx 33$ – $66 R_P$, defined as a region that encompasses the orbits of the four satellites (e.g., Kenyon & Bromley 2019a; Bromley & Kenyon 2020).

The current Pluto–Charon system has a semimajor axis, $a \approx 16.49 R_P$, and an orbital period $P = 6.387$ d (see Stern et al. 2018, and references therein). The orbit is nearly circular (Buie et al. 2012); satellite orbits are also nearly circular (e.g., Buie et al. 2013; Brozović et al. 2015; Showalter & Hamilton 2015). For the numerical calculations considered here, we adopt a much more compact binary, $a \approx 5$ – $10 R_P$, with a range of eccentricities, $e \approx 0.2$ – 0.8 . Tidal evolution models suggest that these compact binaries evolve into the current architecture on time scales of 10^6 – 10^7 yr (e.g., Farinella et al. 1979; Dobrovolskis et al. 1997; Peale 1999; Cheng et al. 2014a; Correia 2020). This time scale is much longer than the 1000 yr evolution time of a typical numerical calculation for the evolution of circumbinary debris. Thus, we ignore tidal evolution.

2.2. Numerical Code

To calculate the evolution of circumbinary solids in the Pluto–Charon system, we run numerical simulations with *Orchestra*, an ensemble of computer codes designed to track the accretion, fragmentation, and orbital evolution of solid particles ranging in size from a few microns to thousands of km (Kenyon 2002; Bromley & Kenyon 2006; Kenyon & Bromley 2006, 2008; Bromley & Kenyon 2011a, 2013; Kenyon & Bromley 2016; Kenyon et al. 2016; Bromley & Kenyon 2020). In this application, we employ several *Orchestra* tools: a multiannulus coagulation code to derive the dynamical evolution of small solids and a gravitational n -body code to enable the solids to respond to the gravitational potential of the central binary. A set of massless tracers enables communication between the coagulation and n -body codes.

Using the *Orchestra* multiannulus coagulation routine, we establish a radial grid, centered on the Pluto–Charon barycenter, of 28 concentric annuli distributed in equal intervals of $a^{1/2}$ between a_{in} (as listed in Table 1) and $a_{max} = 160 R_P$. Each annulus has 80 mass bins with minimum radius $r_{min} = 0.01 \mu\text{m}$ and maximum radius $r_{max} = 1$ m. In a region between a_{in} and a_{out} , we seed the grid with solids having total mass M_0 , material density 1.5 g cm $^{-3}$, surface density $\Sigma \propto a^{-2}$, and a size distribution $n(r) \propto r^{-3.5}$. With these initial conditions, most of the mass lies in the largest objects; the innermost annulus has somewhat more mass than the outermost annulus. Solids have initial pericenter distance q_0 and inclination i_0 as listed in Table 1.

Within the coagulation code, solids evolve due to collisional damping from inelastic collisions and elastic, gravitational interactions. For inelastic and elastic collisions, we follow the statistical, Fokker-Planck approaches of Ohtsuki (1992) and Ohtsuki et al. (2002), which treat pairwise interactions (e.g., dynamical

Table 1. Starting Conditions for Coagulation Calculations^a

Model	a (R_P)	e	a_s (R_P)	a_{in} (R_P)	a_{out} (R_P)	q_0	i_0
1	5.0	0.2	15.0	8.0	32.0	6.0	0.250
2	5.0	0.2	15.0	8.0	32.0	3.0	0.250
3	5.0	0.4	18.3	8.0	32.0	7.0	0.025
4	5.0	0.4	18.3	8.0	32.0	5.0	0.025
5	5.0	0.4	18.3	8.0	32.0	7.0	0.250
6	5.0	0.4	18.3	8.0	32.0	5.0	0.250
7	5.0	0.4	18.3	19.0	32.0	7.0	0.025
8	5.0	0.4	18.3	19.0	32.0	5.0	0.025
9	10.0	0.6	41.5	19.0	32.0	16.0	0.025
10	10.0	0.6	41.5	19.0	32.0	10.0	0.025
11	10.0	0.6	41.5	19.0	32.0	16.0	0.250
12	10.0	0.6	41.5	19.0	32.0	10.0	0.250
13	10.0	0.8	44.6	19.0	32.0	18.0	0.250
14	10.0	0.8	44.6	19.0	32.0	10.0	0.250

^a The columns list the orbital semimajor axis, a in Pluto radii, and eccentricity, e , of the Pluto–Charon binary; the semimajor axis, a_s in Pluto radii, of the innermost stable circular orbit; the initial inner and outer radii, a_{in} and a_{out} , and the pericenter q_0 of circumbinary solids (all in units of R_P); and the initial inclination i_0 of circumbinary solids.

friction and viscous stirring) between all objects. We assume the mass distribution is fixed in time. At the start of each calculation, collisions between m-sized (cm-sized) particles are destructive (accretive). Within a day or two, however, collisional damping reduces relative velocities by factors of 2–3. Although collisions between m-sized objects remain destructive, collisional growth among smaller objects tends to replenish these objects about as fast as they are destroyed. Several tests allowing collisions to grow and fragment particles suggests this process modifies the overall size distribution little over the course of a typical simulation. In these tests, we used the full calculational approach for two sets of calculations, where (i) collision outcomes are derived and debris is distributed among mass bins and (ii) collision outcomes are ignored (maintaining a constant size distribution) but collision rates are used to calculate collisional damping as in set (i). Aside from mass redistribution, the calculations are otherwise identical, using the elastic formalism to treat gravitational interactions that do not result in a physical collision and the inelastic formalism to treat collisional damping. To save resources for the more cpu-intensive n -body calculations, we thus ignore collisional redistribution of mass throughout each calculation.

To allow the e and i of mass bins to react to the gravity of Pluto and Charon, we assign massless tracer particles to each mass bin. Among all mass bins, we assign 448,000 tracers. Within an annulus, each mass bin is allocated ~ 300 tracers (~ 24000 tracers for 80 mass bins). Another set of tracers is assigned to bins

with the most mass per bin. The orbital a for each tracer within annulus i is a random number between $a_i - 0.5\delta a_i$ and $a_i + 0.5\delta a_i$, where a_i is the semimajor axis of the annulus in the coagulation grid and δa_i is the radial width of the annulus. With this selection, tracers have semimajor axes that span the full range between the inner edge and the outer edge of the coagulation grid. Orbital $e_{i,0}$ and $\iota_{i,0}$ for each tracer follow the e_0 and ι_0 for the assigned mass bin. Tracers with $a = a_i$ have pericenters $q_i = q_0 = a_i(1 - e_i)$. Other tracers in annulus i have pericenters q_i that cluster around q_0 : $q_0 - 0.5 \delta a_i (1 - e_i) \leq q_i \leq q_0 + 0.5 \delta a_i (1 - e_i)$. Because δa_i is finite, the tracers have a modest spread in pericenters about the adopted q_0 . Tracers initially have random orbital phases; some tracers are initially near orbital pericenter, while others are near apocenter. Although the midplane of the disk lies in the Pluto–Charon orbital plane, some tracers initially lie within the orbital plane while others begin their evolution out of the orbital plane. Once assigned to a mass bin, tracers may move to another annulus in response to gravitational interactions with Pluto and Charon and the $(de/dt, d\iota/dt)$ derived in the coagulation code. However, tracers do not move among mass bins.

Within the coagulation code, each mass bin k in each annulus i contains a number of particles N_{ik} and a total mass M_{ik} . The average mass of a particle is then $m_{ik} = M_{ik}/N_{ik}$. To allow these particles to respond to the motions of the tracers, we assign a number and total mass of particles to each tracer. With $N_{i,k}^t$ tracers per mass bin, each tracer is responsible for $N_{i,k}' = N_{i,k}/N_{i,k}^t$ coagulation particles. To avoid a tracer ‘carrying’ fractional coagulation particles, the algorithm assigns integer numbers of coagulation particles to each tracer. The mass carried by each tracer follows: $M_{i,k}' = m_{ik}N_{i,k}'$. Summed over all tracers, the mass carried by tracers is the total mass in the coagulation grid. The number and mass of coagulation particles assigned to that tracer effectively follow that tracer as it orbits the system barycenter.

Within the n -body code, tracers are treated as massless particles. As the evolution proceeds, these tracers respond to the gravitational potential of the central binary. In doing so, they generally move to larger distances from the barycenter. While some are ejected, others shift from an annulus i into another annulus j . This shift generates a change in the mass of bins in annulus i and a corresponding (opposite) change in the mass of bins in annulus j . At the end of a time step, the combined set of shifts results in new values for the number and total mass of particles in each mass bin. With new numbers of tracers in each mass bin, $N_{i,k}'$ and $M_{i,k}'$ also change. Thus, the number of particles and the total mass in those particles (but not the average mass of a particle) carried by each tracer varies throughout a calculation.

To choose appropriate starting conditions, we examine outcomes of the [Canup \(2011\)](#) SPH calculations. Among this suite of simulations, ‘successes’ that produce an intact Charon and surrounding debris yield binaries with $a \approx 4\text{--}28 R_P$ and $e \approx 0.1\text{--}0.9$. Systems with larger a have larger e . To span this range efficiently, we consider binaries with $(a, e) = (5 R_P, 0.2)$, $(5 R_P, 0.4)$, $(10 R_P, 0.6)$, and $(10 R_P, 0.8)$. Although these choices do not include the lowest e and highest e systems, they are sufficient to learn how the evolution of the debris depends on the properties of the underlying binary.

Starting points for the debris surrounding Pluto–Charon follow [Canup \(2011\)](#) and models for the giant impact that produced the Moon (e.g., [Ida et al. 1997](#)). From the [Canup \(2011\)](#) calculations, the mass of the debris orbiting Pluto–Charon spans the range from $\sim 10^{20}$ g to $\sim 3 \times 10^{23}$ g. Considering the initial orbital state of the debris, we expect considerable losses from dynamical ejections. Thus, the long-term evolution of a debris field with a mass of 10^{20} g is unlikely to lead to a stable state with a mass comparable to the current mass of the satellites, $\sim 10^{20}$ g. We therefore consider masses of $10^{21} - 10^{23}$ g.

To select initial values of (a, e) for debris particles, we match the final maximum radius of the equivalent circular orbit derived by [Canup \(2011\)](#), $a_{eq,max} \lesssim 20\text{--}30 R_P$; a_{eq} is related to the angular momentum of

orbiting particles (e.g., [Canup 2004, 2011](#); [Nakajima & Stevenson 2014](#); [Bromley & Kenyon 2020](#)):

$$a_{eq} = a(1 - e^2). \quad (1)$$

Because most of the debris lies near Charon (see Fig. 2 of [Canup 2011](#)), we consider calculations with pericenters q_0 (i) near the apocenter of Charon’s orbit around the system barycenter or (ii) within Charon’s orbit. Assigning a range of semimajor axes, $a_d \approx 8\text{--}32 R_P$, for the adopted q_0 yields equivalent circular orbital radii, $a_{eq} \approx 7\text{--}12$, which includes most of the outcomes in Fig. 6 of [Canup \(2011\)](#).

Placing the solids within the mass bins of the coagulation grid requires an adopted surface density distribution $\Sigma(a)$. Independent of the properties of the central binary, we adopt $\Sigma \propto a^{-2}$. Although [Canup \(2011\)](#) does not quote $\Sigma(a)$ for the debris, [Ida et al. \(1997\)](#) consider similar surface density distributions in n-body calculations of the formation of the Moon from an extended disk surrounding the Earth. SPH calculations for the giant impact do not have the resolution to derive a size distribution of small particles. Consistent with the size distributions derived for other impact studies (e.g., [Greenberg et al. 1978](#); [Durda 1996](#); [Durda & Dermott 1997](#); [Leinhardt et al. 2000](#); [Leinhardt & Stewart 2009](#)), we adopt a size distribution $n \propto r^{-3.5}$ for the debris particles. For simplicity, we assume that all particles within annulus i have the same initial eccentricity e_i and inclination i_i . Thus, particles with an initial semimajor axis at the inner edge of the coagulation grid have a smaller e_i than those with a larger initial semimajor axis.

Compared to the central binary, orbiting solids with the adopted initial surface density profile have relatively little total angular momentum. Following [Canup \(2005\)](#), the Pluto–Charon system has an angular momentum $L_{PC} \approx q\Omega(m_P + m_C)a^2/(1 + q)^2$, where q is the mass ratio, Ω is the angular velocity, and a is the semimajor axis (see also [Canup 2011](#)). For the adopted masses, $L_{PC} \approx 3.5 \times 10^{37} \text{ g cm}^2 \text{ s}^{-1}$ ($5 \times 10^{37} \text{ g cm}^2 \text{ s}^{-1}$) for $a = 5 R_P$ ($10 R_P$). The initial configurations of circumbinary solids we consider have $L_s \approx 2 - 4 \times 10^{34} \text{ g cm}^2 \text{ s}^{-1}$ ($M = 10^{21} \text{ g}$) to $L_s \approx 2 - 4 \times 10^{36} \text{ g cm}^2 \text{ s}^{-1}$ ($M = 10^{23} \text{ g}$). For the most massive systems, the angular momentum in orbiting solids is only $\sim 5\%$ to 10% of L_{PC} .

Table 1 summarizes the starting points for each calculation. For each combination of a and e of the central binary, we choose two values for the initial inclination, $i_0 = 0.025$ and 0.25 . The first choice allows for maximum collisional damping throughout the evolution; the second choice provides limits on the ability of collisions to evolve a thick disk into the thin disk required for the growth of satellites ([Kenyon & Bromley 2014b](#); [Walsh & Levison 2015](#)).

Among calculations with $e = 0.4$, we consider two choices for a_{in} : (i) $a_{in} = 8 R_P$ places the solids close to the binary; (ii) $a_{in} = 18 R_P$ places solids farther out in the system. Both of these choices match the $a_{eq,max}$ limits derived in [Canup \(2011\)](#). Aside from testing whether the evolution of solids depends on their initial angular momentum, these calculations allow us to connect results for compact Pluto–Charon binaries with $a = 5 R_P$ to those for wide binaries with $a = 10 R_P$. In the calculations described below, the mass distribution at 1000 yr depends on the ability of collisional damping to prevent ejections by the central binary. When material is close to the binary, collisions and damping are more numerous, but solids spend more time near the binary. More distant solids have lower particle densities and less damping, but these solids spend less time near the binary. Following the evolution for two sets of starting conditions provides insight into the relative importance of collisional damping and gravitational perturbations from the binary.

To give the initial conditions of the models additional context, Table 1 lists a_s the semimajor axis of the innermost stable circular orbit for each model. For the adopted masses of Pluto and Charon, the numerical results of ([Holman & Wiegert 1999](#)) yield

$$\frac{a_s}{a} = 2.175 + 4.58e - 2.152e^2. \quad (2)$$

In the compact binaries we consider, $a_s \approx 15 R_P$ ($18 R_P$) for $e = 0.2$ (0.4). Most of the initial mass then lies outside the innermost stable orbit. The wider binaries have $a_s \approx 42 R_P$ ($45 R_P$) for $e = 0.6$ ($e = 0.8$). At the start of each calculation, most of the mass is on unstable orbits with $a < a_s$.

Our solutions to the evolution equations conserve mass and energy to machine accuracy. Timesteps for the coagulation calculations range from a few seconds at $t = 0$ to 10^6 sec near $t = 1000$ yr. Within the n -body code, the adaptive integrator divides coagulation steps into smaller steps as needed to maintain the integrity of the calculation. With 112 cpus, typical calculations require 30000–50000 timesteps and 2–3 cpu sec per step. Nearly all of this time is spent evolving the dynamics of tracer particles. Over the course of a 1000 yr run, calculations conserve mass and energy to better than one part in 10^{10} .

2.3. Operations

All calculations proceed as follows. For a time step Δt , the coagulation code derives the changes in the e and i of each mass bin from collisions and orbital interactions with all other mass bins. Collision rates are derived from the particle-in-a-box algorithm (e.g., Kenyon & Bromley 2002, 2004, 2008). For each mass bin k in annulus i , the collision rate with solids in mass bin l in annulus j depends on the number density of particles (n_{ik} and n_{jl}), the collision cross-section, the relative velocity, and the overlap of orbits (see sec. 2 of Kenyon & Bromley 2008). When $i = j$, the overlap is 1; otherwise, the overlap is approximately the ratio of the volume of annulus j that lies within the volume of annulus i .

At the end of the coagulation step, each tracer is assigned a target eccentricity e_t and inclination i_t based on its current e_i and i_i and the changes in e and i for its mass bin from the coagulation calculation. These targets result in time derivatives for e and i during a timestep Δt , $de/dt = (e_t - e_i)/\Delta t$ and $di/dt = (i_t - i_i)/\Delta t$. Before the n -body step, tracers are also assigned new numbers and masses of particles based on the number and mass within each mass bin. Although the n -body code does not use this information, each tracer carries a changing mass of solids based on the evolution of solids in the coagulation grid.

Within the n -body step, we solve the equations of motion for a set massless tracers orbiting the Pluto–Charon binary, using an adaptive algorithm with sixth-order time steps, based on Richardson extrapolation (Bromley & Kenyon 2006, 2011a). The code follows objects in the center-of-mass frame, calculating forces by direct summation. Aside from the extensive tests reported in Bromley & Kenyon (2006, 2011a), the code has been used for investigations of migration (Bromley & Kenyon 2011b), Saturn’s rings (Bromley & Kenyon 2013), and the formation and stability of the Pluto–Charon system system (Kenyon & Bromley 2014a; Bromley & Kenyon 2015a; Kenyon & Bromley 2019a,b,c; Bromley & Kenyon 2020).

Throughout the n -body calculations, tracers evolve with their derived de/dt and di/dt and respond to the gravitational potential of Pluto and Charon. Orbits evolve with ~ 200 steps per binary orbit. The tracers’ eccentricity e and inclination i are shifted incrementally at rates set by the coagulation code. These changes to e and i are implemented by small adjustments to the direction of travel and (if necessary) incremental shifts in position, without affecting the other osculating orbital elements.

At the end of the n -body step, tracers have new positions, velocities, and orbital elements a , e , and i . Tracers with new a that places them outside their ‘old’ annulus are placed in new annuli; the number and mass of particles assigned to that tracer move out of the old mass bin into a new mass bin within the new annulus. Some tracers collide with Pluto or Charon; others are ejected beyond the outer limits of the n -body calculation space, $a \gtrsim 1000 R_P$. After these tracers are deactivated for the remainder of the calculation, the coagulation particles associated with these tracers are removed from the coagulation grid. When an active tracer has a semimajor axis outside of the coagulation grid, its mass is removed from the old annulus and

is not placed in a new annulus. If that tracer returns to the grid before a collision with Pluto–Charon or ejection, the mass that it carries also returns to the grid.

Although assigning tracers to annuli based on their current position (x, y, z) seems reasonable, placement based on a is more in the spirit of the coagulation code. The collision and Fokker-Planck algorithms derive rates based on particle volumes, $V = 4\pi a \Delta a H$, where $\Delta a \approx \delta a + ea$, δa is the physical width of the annulus, and H is the vertical scale height which depends on the orbital inclination i (Kenyon & Bromley 2008). For circumbinary solids, the physical extent of particle orbits is much larger than the physical width of each annulus. Thus, placing tracers in annuli according to a recovers the correct volume for calculations of collision and stirring rates.

New orbital elements for tracers inform the e and i of mass bins in the coagulation code. Within each mass bin, the median e and i and their inter-quartile ranges for tracers assigned to that mass bin establish the new e and i for the mass bin. The inter-quartile ranges allow for quantitative monitoring of the accuracy of the median in measuring the typical e and i for a set of tracers. Typically, the inter-quartile ranges are small.

This sequence provides a closed-loop algorithm that allows the mass bins and the tracers to respond to the gravity of Pluto–Charon and the orbiting solids. The coagulation particles tell the tracers how to react to solid material orbiting Pluto–Charon. In turn, the tracers tell the solid material how to react to Pluto–Charon. As long as time steps are not too long, the lag between the coagulation and n -body steps does not introduce significant offsets in the evolution of the mass bins and the tracer particles.

To maximize the accuracy of this approach, the codes have a set of control parameters. During the coagulation step, changes in the (e, i) of particles in each mass bin never exceed 1%. When changes exceed this limit, the time step is reduced and repeated. During the n -body step, the adaptive integrator adjusts the number of adaptive steps per Pluto–Charon orbit to track collisions between tracers and Pluto and Charon. Several examples in Bromley & Kenyon (2006) illustrate the accuracy of the n -body code. After completion of the n -body step, algorithms within the coagulation code verify that changes in the median (e, i) among tracers within a mass bin are still less than 1% and that the changes in the inter-quartile ranges among the tracers is less than 2%. Larger changes trigger a reduction in the time step. As an independent check on this process, we compared results with the maximum level of changes set at 0.5% and could not measure a significant difference between outcomes over 1000 yr of evolution.

3. RESULTS

For each of the starting conditions in Table 1, we performed simulations with five initial masses, $M_0 = 10^{21}$ g, 3×10^{21} g, 10^{22} g, 3×10^{22} g, and 10^{23} g. All calculations follow the same evolutionary sequence. During their first pass around the barycenter, tracers get a push from the central binary. Concurrently, collisions damp the orbital e and i of every tracer. For the rest of a calculation, the behavior of tracers depends on the relative importance of damping and gravitational accelerations that try to remove solids from the region where circular orbits are unstable. For some tracers, damping circularizes their orbits at large a and reduces their inclinations before the binary ejects them from the system. Among other tracers, collisions fail to circularize orbits. Although tracers with large initial i damp into the orbital midplane of the central binary, many are ejected through the midplane beyond the system’s Hill sphere.

After 1000 yr of evolution, most surviving tracers lie within a disk surrounding the binary. These tracers have $e \lesssim 10^{-2}$. The disk has a sharp inner edge, where solids follow orbits just outside the unstable region, $a \gtrsim a_s$. The peak in the disk surface density (Σ) lies at somewhat larger distances from the binary and is

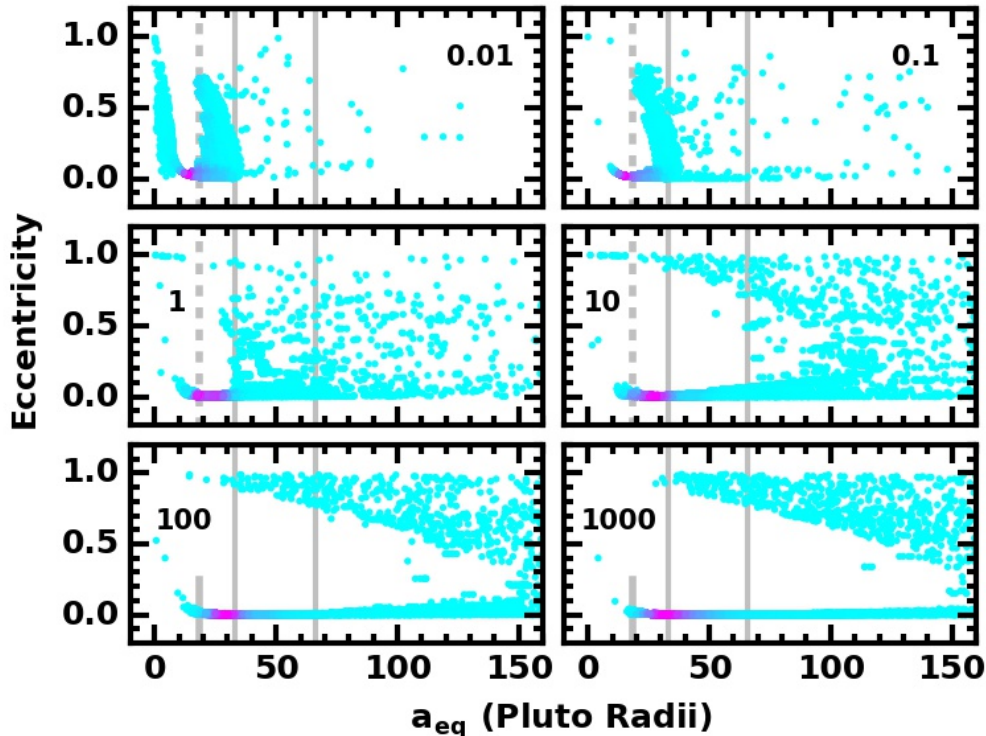


Figure 1. Snapshots of the time evolution of material orbiting a central binary with $a = 5 R_P$ and $e = 0.4$. Each panel shows the positions of solids in the (a_{eq}, e) plane for $q_0 = 7 R_P$ and the times (in yr) indicated in the legend. Cyan points show positions of individual tracer particles. Magenta points denote regions of high density; the intensity of the color provides a measure of the density. Initially, most of the solids lie on high e orbits with pericenter close to the apocenter of Charon’s orbit. As the calculation proceeds, collisional damping places more and more solids into a disk. Within the disk, the position of peak surface density moves outward with time.

within or close to the satellite zone. Beyond the peak surface density at $a = a_m$, Σ declines rather steeply, $\Sigma \propto a^{-p}$ with $p \approx 3-6$. Among tracers outside of the disk, most have $i \approx 0$; a few have $i \approx 0.05-0.25$. Close to the binary ($a_{eq} \approx 20-40$), survivors outside of the disk have $e \approx 1$. Tracers with larger a_{eq} have a range of e ; this range grows with increasing a_{eq} . At $a_{eq} \approx 150-200 R_P$, some tracers have $e \approx 0.01-0.1$.

To illustrate this evolution, Fig. 1 shows snapshots of the eccentricity distribution of tracers for selected times in the evolutionary sequence of model 5 ($a = 5 R_P$, $e = 0.4$, $a_{in} = 8 R_P$, $a_{out} = 32 R_P$, $q_0 = 7 R_P$, and $v_0 = 0.25$) with an initial mass of 10^{21} g. To place these results in the context of previous studies, we plot e (later, i) as a function of a_{eq} instead of the semimajor axis. Initially, solids have large e ; a_{eq} is then much smaller than the semimajor axis. As collisional damping reduces e , $a_{eq} \approx a$.

In this calculation, solids initially have a broad range of e , from $e \approx 0.1$ at $7 R_P$ to $e \approx 0.8$ at $32 R_P$. Without collisional damping, all of these orbits are unstable. However, collisional damping acts rapidly to circularize these orbits. After 0.01 yr, some solids lie in a thin ring with $a_{eq} \approx 10-15 R_P$ (upper left panel of Fig. 1). Concurrently, the central binary attempts to eject particles from the system, placing them within the ensemble of tracers at $a_{eq} \approx 20-30 R_P$ and $e \lesssim 0.6$ in this panel. A third set of tracers has not had enough time to evolve; these inhabit a group with $a_{eq} \lesssim 10 R_P$ and $e \lesssim 1$.

As the evolution proceeds, the tracers with initially small a_{eq} move to larger a_{eq} (Fig. 1, upper right panel). Some of these lie within the narrow ring at small a_{eq} ; others lie within a fledgling disk extending from $\sim 20 R_P$ to $\sim 100 R_P$. Almost all of the rest make up the swath of particles with a range of e at $a_{eq} \approx 20\text{--}40 R_P$. However, there are a few particles with large a_{eq} and large e . These solids are on their way out of the Pluto–Charon system.

From 1 yr to 1000 yr, the evolution turns into a competition between collisional damping and dynamical excitation by the central binary. Throughout each orbit, collisional damping tries to circularize particle orbits. Solids with large e receive a kick from the binary near the pericenters of their orbits. This combination of processes tends to push particles onto more circular orbits at larger a . As the system evolves, solids separate into the two groups illustrated in the middle and lower panels of Fig. 1. A group of particles with $e \approx 0$ forms a thin disk with a peak surface density at $20\text{--}40 R_P$. This peak gradually moves to larger a_{eq} . The second group of particles lies within the broad swath at the upper right of each panel, with large e at small a_{eq} and small e at large a_{eq} . Within this swarm, collisional damping acts to prevent ejections; combined with kicks from the binary, particles evolve to larger and large a_{eq} within the disk. For roughly 2/3 of the particles, collisional damping is too slow; these particles are eventually ejected from the system. Of the remaining solids, nearly all lie within the disk. With a final mass of 3×10^{20} g, this disk has sufficient mass to produce a few larger objects with the combined mass of the current satellites ($\sim 10^{20}$ g, Kenyon & Bromley 2019b).

In the lower right panel of Fig. 1, tracer particles outside the disk constitute only 6% of the remaining mass in the system. Based on the evolution from 100 yr to 1000 yr, we estimate that 1/3 to 1/2 of this material will be placed into the disk at $a \gtrsim 200 R_P$. Because these solids will contribute negligibly to the disk in the satellite zone, we halted the calculation at $t \approx 1000$ yr.

The evolution of the inclination closely follows the evolution of the eccentricity (Fig. 2). Initially, all tracers have $i = 0.25$. In only a few days, a substantial fraction of particles has small inclination and lies within the narrow ring at $10\text{--}20 R_P$ or a swarm of high inclination particles with $a_{eq} \approx 20\text{--}30 R_P$. Over the next year, many particles damp into the disk at radii $a_{eq} \approx 15\text{--}150 R_P$. Others remain in a high inclination group that moves out to $40\text{--}50 R_P$. Aside from a few outliers, the high inclination group disappears from 10 yr to 1000 yr. All other tracers lie within the disk.

At 1000 yr, the disk in Fig. 1–2 is well-defined and fairly stable. Inside $100 R_P$, the disk contains a little more than twice the mass of the Pluto–Charon satellite system, $M_d(a \leq 100 R_P) \approx 2.5 \times 10^{20}$ g. With low eccentricity, $e \lesssim 0.01$, and lower inclination, $i \lesssim 0.001$, low mass solids will steadily grow into larger and large objects and eventually form a robust satellite system (Kenyon & Bromley 2014b).

Fig. 3 shows several snapshots of the surface density profile of the disks in Figs. 1–2. After the first year, the surface density peaks at $10\text{--}20 R_P$ from the system barycenter. For a binary with $a = 5 R_P$ and $e = 0.4$, nearly all orbits in this region are unstable (Eq. 2, Table 1). As the evolution proceeds, the binary pushes material to larger distances; collisional damping reduces orbital e and i to keep this material in the system. Over the next 1000 yr, the surface density at $10\text{--}20 R_P$ drops from close to 100 g cm^{-2} to less than 0.1 g cm^{-2} .

While the binary ejects solids from the unstable region, damped solids fill the disk beyond $50 R_P$. From 0.1 yr to 1 yr, the surface density at $40\text{--}100 R_P$ grows by a factor of 100, from $10^{-3}\text{--}10^{-5} \text{ g cm}^{-2}$ to $10^{-1}\text{--}10^{-3} \text{ g cm}^{-2}$. During the next 1000 yr, the surface density in the disk increases by another factor of 10. With little change in Σ during the last 100–200 years of evolution, the surface density profile of the disk is stable at the end of this calculation.

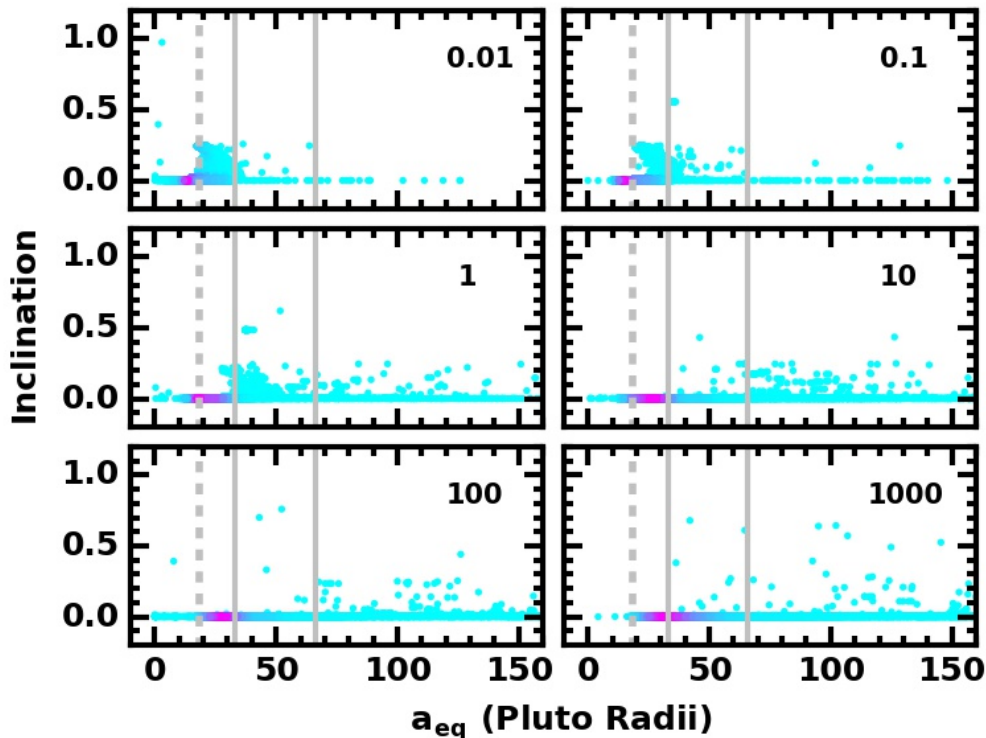


Figure 2. As in Fig. 1 for the inclination. As time proceeds, particles with $i \approx 0.25$ move to large a_{eq} . Some solids rapidly damp into a thin disk with a small scale height. Others are ejected out of the system with a range of i relative to the orbital plane of the central binary. At the end of the calculation, most of the remaining solids lie within the vertically thin disk; a few with large i are on their way out of the system.

Throughout the evolution, material in the inner part of the disk at $10\text{--}20 R_P$ is more likely to be ejected than to remain in the disk. At $0.1\text{--}1$ yr, the inner disk contains $\sim 10^{21}$ g of solids. After 1000 yr, only $\sim 3 \times 10^{20}$ g remains at $20\text{--}35 R_P$. Although some inner disk material finds stability in the outer disk at $50\text{--}150 R_P$, these solids are a small fraction of the material ejected from $10\text{--}25 R_P$. At the end of this calculation, $\sim 10^{20}$ g ($\sim 10^{19}$ g) lies at $40\text{--}60 R_P$ ($60\text{--}120 R_P$). Overall, the mass of the solids falls from the initial 10^{21} g to a final 3.5×10^{20} g. Nearly all of the mass remaining at 1000 yr is in the disk.

In addition to a redistribution of mass, the surface density profile gradually becomes smoother with time. After a few weeks of evolution, the profile is irregular and varies chaotically beyond $50 R_P$. Within a year, the profile is smoother, with a wavy appearance beyond $30 R_P$. These waves probably result from the action of the central binary, which perturbs solids as collisional damping circularizes their orbits. By 1000 yr, the surface density profile is fairly featureless, with only a few small-scale wiggles superimposed on a monotonically decreasing profile.

The model 6 calculations follow nearly the same evolution shown in Figs. 1–3. With a smaller q_0 , solids have a larger initial e but the same initial i . As the binary attempts to kick solids out of the system, collisional damping tries to circularize their orbits. Solids that cross Charon’s orbit feel larger gravitational perturbations than those that always stay outside of the binary orbit. Larger kicks make it harder for damping to reduce e and i and to keep these particles in the system. Despite the actions of the central binary, damping reduces inclinations fairly rapidly, generating a thin disk in the Pluto–Charon orbital plane within

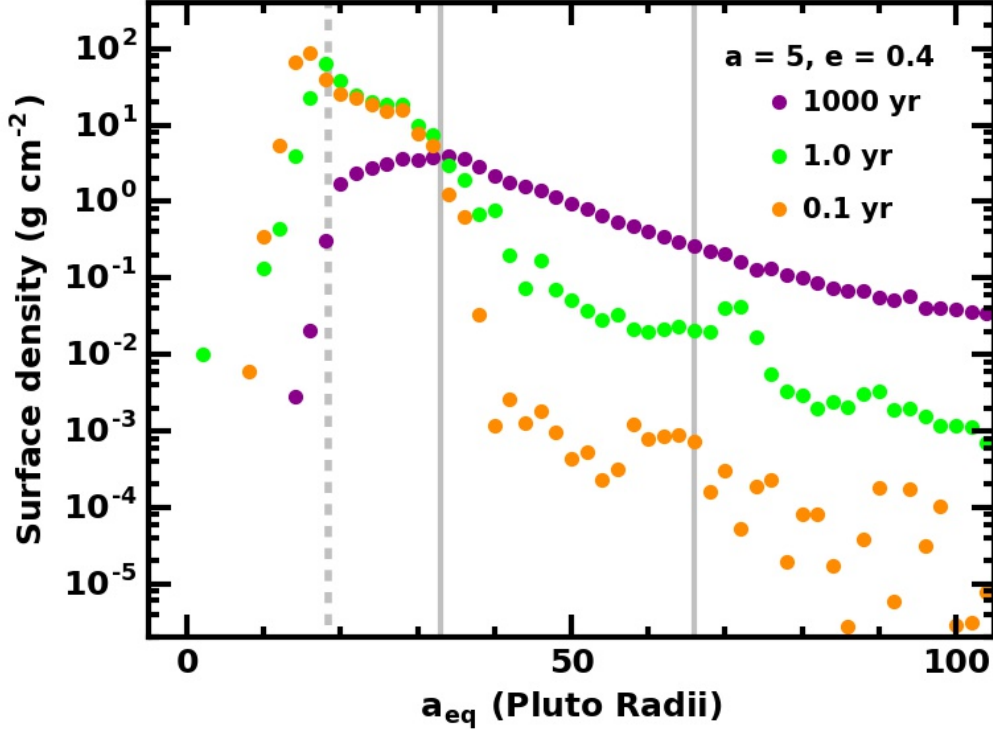


Figure 3. Surface density profiles at 0.1 yr (orange points), 1 yr (green points), and 1000 yr (purple points) for the calculation shown in Figs. 1–2. The vertical dashed line marks the position of the innermost stable circular orbit around the central binary. Vertical solid lines indicate the extent of the satellite zone.

1 yr. With more material in the midplane at all times, damping rates grow, enabling a larger fraction of existing particles to remain in the system.

Compared to model 5, these calculations exhibit two interesting features. For the low mass calculations ($M_0 = 1-3 \times 10^{21}$ g), collisional damping tends to lag gravitational perturbations from the binary. Although e and i drop with time, perturbations from the binary push particles to larger and larger a . At larger a , the solids occupy a somewhat smaller volume due to the smaller e (which limits their radial excursions) and the smaller i (which limits their vertical excursions), which increase rates and hence the effectiveness of damping. Combined with smaller perturbations from the binary at large a , enhanced damping allows formation of a disk at $a \gtrsim 30-40 R_P$. After 1000 yr, remaining solids have formed a disk with a size similar to the solids in model 5. However, these disks have less mass than the model 5 disks. Their shallower surface density distributions have a larger fraction of mass at larger distances, a characteristic of the initially larger kicks from the central binary and the ineffectiveness of collision damping at small semimajor axis, a_{lessima_s} .

In contrast, calculations with the model 6 initial conditions and large initial masses are able to retain a larger fraction of their initial mass. When the initial mass is larger, collisional damping – which scales as the square of the mass – is more effective. The vertical extent of the swarm decays more rapidly into the midplane; more particles lie within the dense ring at $20-30 R_P$ and within the nascent disk at larger distances. As the calculations proceed, the binary still manages to eject most of the initial mass from the system. However, the final disk masses are remarkably similar to those in model 5. Although there are

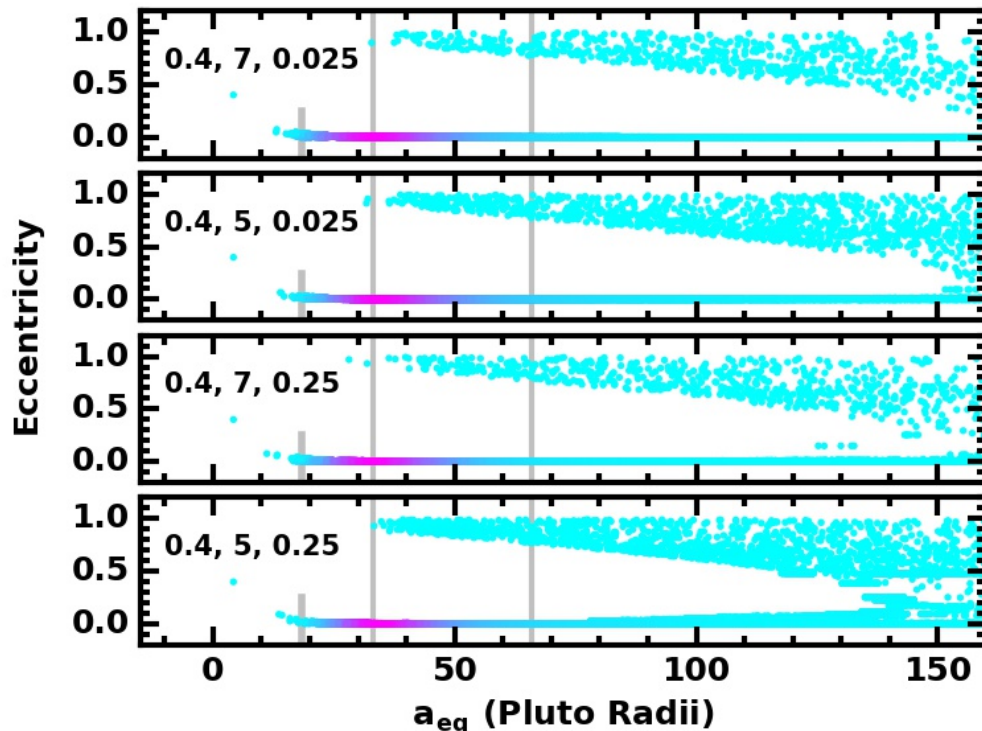


Figure 4. Distribution of surviving particles in (a_{eq}, e) space at 1000 yr for calculations with the model 3–6 initial conditions and $M_0 = 10^{21}$ g. Cyan points indicate the positions of individual tracers. Magenta pixels denote regions of high density; the intensity of the color provides a measure of the particle density in each pixel. Labels list e for the central binary, q_0 , and i_0 . In all panels, the cyan and magenta points delineate an extended disk with an inner edge at $\sim 20 R_P$, a maximum density at 30–40 R_P , and an outer edge at 200–300 R_P . The morphology of the points in the upper and the lower middle panels for $q_0 = 7$ demonstrates that the outcome is fairly independent of i_0 . Comparison of the upper two and lower two panels illustrate the impact of q_0 . When $i_0 = 0.25$, the outcome at 1000 yr is fairly independent of q_0 . At 1000 yr, systems with larger i_0 have more particles at higher eccentricity than those with smaller i_0 . Above the disk, particles in limbo have $e \approx 1$ at small a_{eq} and a broad range of e at large a_{eq} . Over time, some of these particles will be incorporated into the disk; the central binary will eject others from the system.

modest differences among the calculations, massive disks with the model 5 starting conditions have disks with a physical structure close to the structure of disks with the model 6 parameters (see Table 2).

Reducing the initial inclination of the particles ($i_0 = 0.025$, models 3–4) has a modest impact on the results. With a smaller inclination, the solids occupy a smaller volume. Collisional damping is then more effective. At the same time, particles on eccentric orbits see larger perturbations in the gravitational potential due to the central binary. As particles experience larger accelerations from the binary, collisional damping circularizes their orbits somewhat more rapidly compared to solids in the model 5–6 calculations. Overall, these two processes approximately cancel: the model 3 and 4 calculations retain roughly the same amount of mass as their model 5 and 6 counterparts; the overall extent and mass distribution within the disks are also fairly similar.

Fig. 4 compares the distribution of e as a function of a_{eq} for surviving particles at 1000 yr in calculations with the model 3–6 initial conditions and $M_0 = 10^{21}$ g. The upper two panels show results for models 3 and 4; the lower two panels plot outcomes for models 5 and 6. All four panels have a similar morphology.

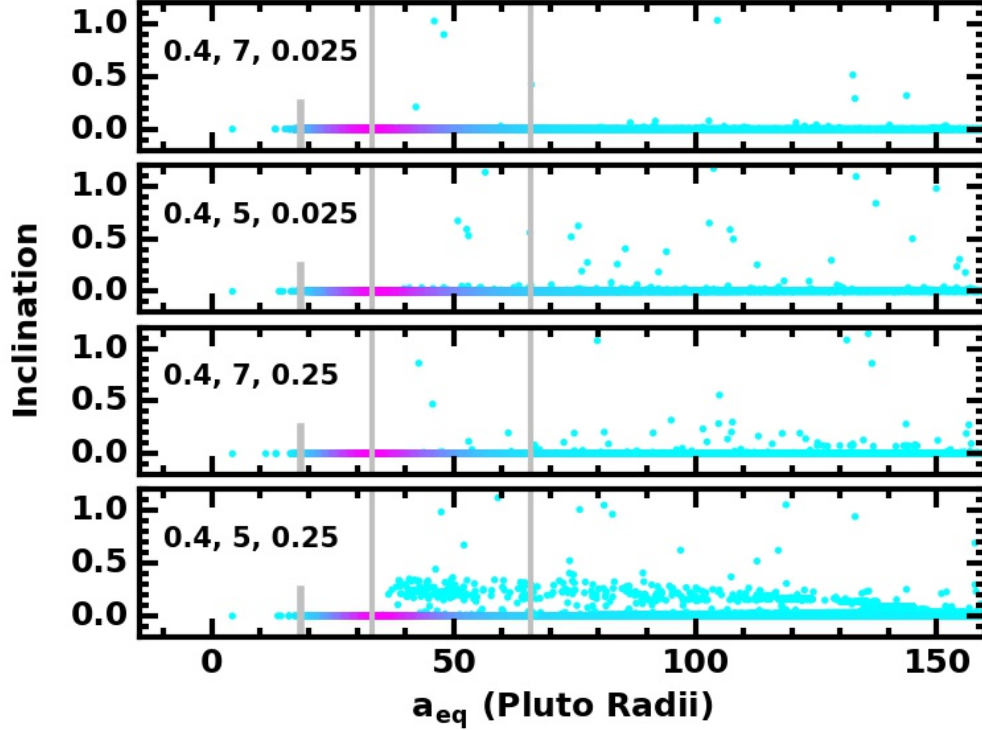


Figure 5. As in Fig. 4 for the inclination. At 1000 yr, all calculations show a clear disk in the midplane of the Pluto–Charon binary; the disk begins at an inner edge of $20 R_P$, reaches peak surface density at $30\text{--}40 R_P$, and extends to $200\text{--}300 R_P$ beyond the right edge of the panels. Above the disk, particles in limbo have $i \approx 0.25$ at small a_{eq} and smaller i at large a_{eq} . Over time, some of these particles will be incorporated into the disk; the central binary will eject others from the system.

A large swarm of particles lies in the orbital plane of the binary. The inner edge of this distribution has $a_{eq} \approx 20 R_P$; the outer edge is beyond the right limits of the plot. Each swarm has a density maximum at $30\text{--}40 R_P$. The position of the density maximum varies little from one panel to the next; there is no obvious dependence of the disk morphology on q_0 or e_0 .

In all four panels, there is a second swath of particles extending from $(a_{eq}, e) = (30, 1)$ to larger a_{eq} . At large a_{eq} , the particles have a broad range of eccentricity, $e \approx 0.2\text{--}1$. This subset of particles is in limbo: collisional damping has kept them within the Pluto–Charon system, but continued kicks from the binary have prevented them from becoming incorporated into the disk. Panels for $q_0 = 7 R_P$ clearly have fewer particles in this swarm than those with $q_0 = 5 R_P$. At $a_{eq} \approx 140\text{--}160 R_P$, there is also a clear gap between the disk particles and those outside the disk. In the panels for $q_0 = 5 R_P$, this gap is occupied by other particles in limbo.

Based on the evolution up to 1000 yr, we anticipate that many of the particles in limbo will eventually become part of the disk. In all of these calculations, the lower edge of the swarm in (a_{eq}, e) space forms a nearly straight line from $(a_{eq}, e) \approx (35, 1)$ to $(a_{eq}, e) \approx (140\text{--}180, 0.1\text{--}0.2)$. Surviving solids above this locus will have final disk radii beyond $140\text{--}180 R_P$ and contribute little mass to the disk.

Fig. 5 repeats Fig. 4 for the inclination. As in Fig. 4, all of the panels display a similar morphology. A large swarm of particles with $i \approx 0$ extends from $\sim 20 R_P$ to beyond $150 R_P$. With $i \approx 0$, these disk particles lie

in the Pluto–Charon orbital plane. Peak surface density within this disk is at 30–40 R_P . Unlike Fig. 4, the upper three panels in Fig. 5 show few particles outside of the Pluto–Charon orbital plane. Although some of these survivors might eventually become part of the disk, the binary will probably eject most of them.

The lowest panel in Fig. 5 has a large group of particles from $(a_{eq}, i) = (40, 0.25)$ to $(a_{eq}, i) = (150, 0)$. These particles are also in limbo; the competition between collisional damping and excitation from the binary is more balanced than for the stable particles already in the midplane and for the less fortunate solids ejected from the system. From an analysis of the evolution at 10–1000 yr, particles within this swath will eventually land in the disk at large a_{eq} or will be ejected from the Pluto–Charon system. The trend in i with a_{eq} indicates how evolution into the disk proceeds: as damping reduces i , the binary pushes a particle to larger a_{eq} . The location where the swath crosses the midplane is the location where particles damp to roughly zero inclination. As the evolution proceeds beyond 1000 yr, we expect that some of particles with higher inclination will damp into the disk at a_{eq} larger than 150 R_P . Because our main interest is on the location of solids near the satellite zone, we chose not to follow this evolution in detail.

Fig. 6 compares the surface density distributions for models 3–6 and $M_0 = 10^{21}$ g. All exhibit the same general trend: a sharp edge at 20 R_P , a clear maximum at 30–35 R_P , and a gradual decline out past 150 R_P . Aside from this trend, there are several clear differences. Models with $q_0 = 7 R_P$ ($q_0 = 5 R_P$) have a broad (narrow) peak. The shape and location of the peak does not depend on i_0 . At large a_{eq} , the decline of the surface density is fairly independent of q_0 and i ; in all calculations Σ declines by a factor of 300–500 from 30–35 R_P to 150 R_P .

Although three of the surface density distributions have a monotonic decline from 35 R_P to 150 R_P , results for model 6 show a clear wave at 80–150 R_P . In this example, the surface density profile evolves as shown in Fig. 3. After one year, disk material lies close to the innermost stable orbit. As the system evolves, most of these solids are ejected. However, some solids in the inner disk move onto stable orbits well outside the innermost stable orbit. As the outer disk stabilizes, the surface density has a wavy appearance generated by the interplay between the binary trying to excite the orbits and collisional damping working to maintain solids on circular orbits. During these interactions, solids find a stable a and e . The time scale for the waves to damp (and for the surface density to become smooth) depends on the properties of the inner binary and the initial q of circumbinary solids. In less eccentric binaries, the waves damp more rapidly compared to the waves in disks surrounding more eccentric binaries. Similarly, waves generated by solids with initially smaller q take longer to damp than those with initially larger q .

In the example shown in Fig. 6, the wave results from particles with initially large q . At later times, the particles have modest eccentricity, $e \lesssim 0.1$, and negligible inclination, $i \lesssim 10^{-2}$; collisional damping has not quite circularized their orbits. These particles are visible as a thickening of the e vs a_{eq} distribution at large a_{eq} in the lowest panel of Fig. 4. In the other calculations shown in Fig. 4, collisional damping operates somewhat faster and circularizes nearly all of the orbits in 1000 yr. In model 6, another 1000 yr of evolution would allow collisional damping to finish circularizing the orbits of these particles; the surface density distribution will then follow the other results more closely.

Although mean-motion resonances (MMRs) may eventually appear in these surface density distributions, none are present after 1000 yr of evolution. For the calculations illustrated in Fig. 6, low order MMRs such as the 3:1 to 7:1 lie inside the innermost stable orbit for an $e = 0.4$ binary. In these four examples, the 14:1, 15:1, 16:1, and 17:1 MMRs at 29–33 R_P are within the region of peak surface density at $\sim 30 R_P$. However, the time scale for MMRs to develop in this region is $\gtrsim 0.1$ Myr (see, for example Kenyon & Bromley 2019a). As the binary expands on similar time scales (e.g., Farinella et al. 1979; Dobrovolskis

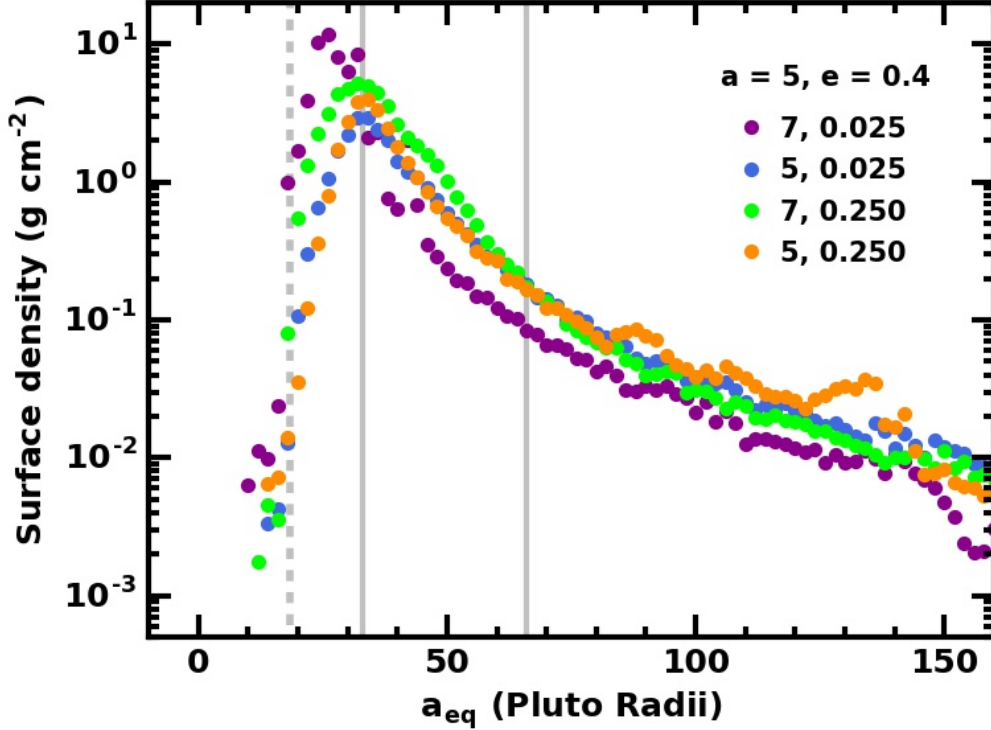


Figure 6. Surface density distributions for model 3–6 calculations with $M_0 = 10^{21}$ g. The legend indicates (a, e) for the central binary and (q_0, v_0) for the solids in each calculation. Vertical grey lines show the boundaries of the satellite zone. The surface density rises from a sharp inner edge at $\sim 20 R_P$ to a sharp peak at $35 R_P$; the surface density then falls over two orders of magnitude from the peak to $150 R_P$. Ripples in the surface density at $80\text{--}150 R_P$ for the model with $(q_0, v_0) = (7, 0.25)$ are typical of disks that have not quite settled into an equilibrium state.

et al. 1997; Peale 1999; Cheng et al. 2014a; Correia 2020), lower order MMRs will sweep through this region (Ward & Canup 2006; Lithwick & Wu 2008; Cheng et al. 2014b). Collisional damping can stabilize solids against the perturbations induced by these MMRs (Bromley & Kenyon 2015b).

To illustrate the impact of the initial a_i and q_0 on the evolution of solids, Fig. 7 plots the “survivor fraction” as a function of the initial semimajor axis of solids. For solids with initial semimajor axis at $8\text{--}10 R_P$, from 2% ($M_0 = 10^{23}$ g) to 10% ($M_0 = 10^{21}$ g) remains in the system after 1000 yr. These fractions are amazingly independent of the initial q . At $10\text{--}20 R_P$, the survivor fraction remain fairly independent of initial a and q for a given initial mass. At $20\text{--}25 R_P$, however, systems with larger initial q retain a larger and larger fraction of solids as the initial a increases. In contrast, systems with an initial q at $5 R_P$ have a low survivor fraction independent of initial a . Clearly, systems with larger q retain much more of their initial mass than those with smaller q .

The variation of survivor fraction with initial a and q is a result of the interplay between gravitational forcing from the binary and collisional damping. In the restricted three-body problem, perturbations in the potential due to the binary are a strong function of the semimajor axis, with leading terms $\propto a^{-2}$ inside Charon’s orbit and $\propto a^{-3}$ outside the binary (Lee & Peale 2006; Leung & Lee 2013; Bromley & Kenyon 2015a, 2021). Near the innermost stable orbit, the binary pumps up the eccentricity of circumbinary solids, or ejects them directly during strong, close encounters. For a Pluto–Charon binary with $a = 5 R_P$ and $e =$

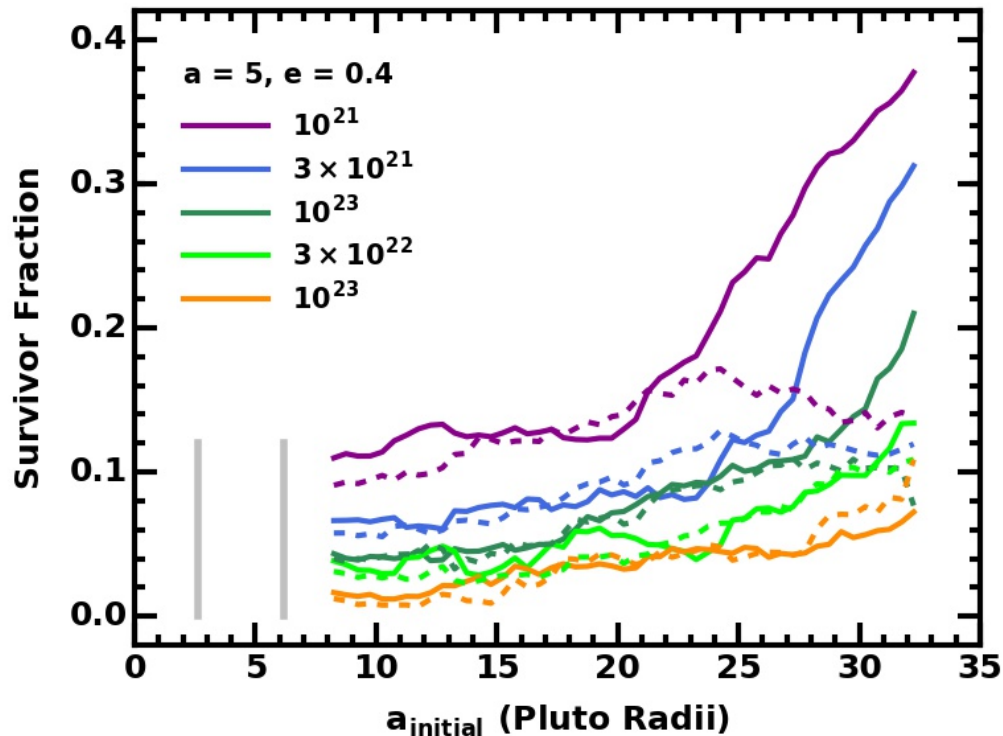


Figure 7. Fraction of tracers that survive 1000 yr of evolution as a function of their initial semimajor axis for a binary with $a = 5 R_P$, $e = 0.4$, and various initial masses as indicated in the legend. Solid (dashed) curves show results for systems of solids with pericenters near the apocenter of Charon’s orbit (with pericenters midway between the apocenter and pericenter of Charon’s orbit), indicated by the vertical grey lines). Although the ability of the central binary to solids at 8–25 R_P is fairly independent of q_0 , the retention of solids on more distant, more eccentric orbits depends on q_0 .

0.4, the innermost stable orbit is at $a = 18 R_P$; inside this distance, objects on completely circular orbits cannot survive. Solids on eccentric orbits are rapidly ejected. At larger distances, near the peak of the surface density distribution ($a \approx 35 R_P$), damping is fast enough to preserve solids even when their initial eccentricity is high.

Collisional damping depends on the particle density n and the relative velocity v as $n^2 v$. Initially, particles have large e and occupy a large volume; collisional damping rates are then low. The binary proceeds to eject particles by increasing their a and e . As a grows, however, particles spend less time near the binary. At large a , collisional damping dominates perturbations from the central binary. Damping lifts the pericenters of particle orbits, reducing binary perturbations near pericenter. As orbits circularize, n^2 grows faster than v falls; damping rates grow rapidly. Throughout circularization, particles orbit at larger a due to binary forcing, but with smaller e and larger q . Although moving to larger a reduces perturbations from the binary and damping rates, damping tends to dominate when particles have larger a and smaller e . Thus, orbits circularize at semimajor axes much larger than the original semimajor axis.

Although damping is effective at large a when solids have pericenters near Charon’s apocenter (e.g., $q \approx Q_c$), the binary dominates when $q \ll Q_c$ (e.g., Lee & Peale 2006; Leung & Lee 2013; Bromley & Kenyon 2015a, 2021). Inside Charon’s orbit, most orbits are chaotic except for a few stable regions near Pluto (Winter et al. 2010; Giuliatti Winter et al. 2013, 2014, 2015). When solids with $a \gtrsim 18 R_P$ travel

inside Charon’s orbit, strong, repeated interactions with the binary carry a high risk of collision or ejections. For some tracers, damping raises the pericenter sufficiently to escape these outcomes. For most tracers, however, close encounters dominate; the binary ejects the tracer from the system before damping acts. In this way, solids with initial $q \ll Q_c$ have a small survivor ratio independent of initial a .

Tracer survival also depends on the initial mass of the swarm. Because damping depends on N_{ik}^2 , systems with more mass damp more effectively. With all orbits passing close to (or within) the binary, very efficient damping has the drawback of circularizing many orbits at semimajor axes $a \lesssim a_s$. These orbits are unstable; thus, these particles are ejected rapidly. More massive systems of solids damp a larger fraction of their mass inside the region where orbits are unstable. In this way, more massive systems lose a larger fraction of their initial mass to dynamical ejections.

Calculations with the model 7–8 parameters begin with the same binary parameters and the same initial masses and inclinations as models 3–4, but have a different radial distribution of solids. With an inner radius of $19 R_P$ instead of $8 R_P$, all of the solids begin with large eccentricities, $e \approx 0.63$ – 0.75 for model 7 and $e \approx 0.74$ – 0.84 for model 8. Models with larger initial e allow the binary more chances to eject particles before collisions circularize orbits. Compared to the results for model 5 (model 6), the model 7 (model 8) calculations retain less mass in the circumbinary disk. Aside from the lower mass, the disks have roughly the same extent and radial distribution of mass in all of the models (see Table 2).

Despite differences in the amount of retained mass, all of the model 7–8 calculations evolve in a similar way. Solids near the center-of-mass receive an immediate kick from the binary. For solids farther away, collisional damping has a few days to reduce e and i before the gravity of the binary impacts their trajectories. After the first few orbits, collisional damping eases some solids into a circumbinary ring at 20 – $30 R_P$ and a few others into a disk at 30 – $100 R_P$. As the ring and disk form, the binary ejects many other solids from the system. Within the first year or two, the ring and disk are fairly well-defined; as time goes by, the ring expands and damping places more solids into the disk.

Fig. 8 compares the remarkably similar surface density distributions at $t = 1000$ yr for models 3, 4, 7, and 8 and $M_0 = 10^{21}$ g. All have negligible mass inside $20 R_P$, a sharp peak at 30 – $40 R_P$, and a steep decline in Σ from the peak to 200 – $300 R_P$. Distributions for models 7 and 8 are somewhat wavier at 100 – $200 R_P$ than for models 3 and 4. Another 1000 yr of damping would smooth out any waves in all of the surface density distributions. Despite the wave, it is clear that these systems have much of their mass inside the satellite zone.

Calculations with larger initial mass in solids follow the same evolution path as those with the lowest mass. When M_0 is larger, collisional damping is more effective; orbits circularize more rapidly. Because the solids evolve towards orbits with smaller a and shorter periods, the binary has more opportunities to eject solids from the system. Over the first few years of evolution, systems with larger M_0 suffer more ejections than those with smaller M_0 . Survivors are placed on orbits with larger a .

Fig. 9 shows density distributions at 1000 yr for model 5 calculations with different M_0 . At $a_{eq} = 10$ – $25 R_P$, the five calculations have a sharp edge, where Σ grows by 3–4 orders of magnitude. Each disk has a clear maximum in Σ at 30 – $60 R_P$; the position of the peak moves to larger a_{eq} when M_0 is larger. Beyond the peak, Σ falls rapidly with a_{eq} . For several calculations, the drops in σ is somewhat wavy. Over time, these waves decline in amplitude.

In these calculations, the slope of the surface density distribution is a strong function of the initial mass. In systems with the smallest M_0 (10^{21} g), Σ roughly follows a power-law with slope $p \approx 3.5$. As the initial

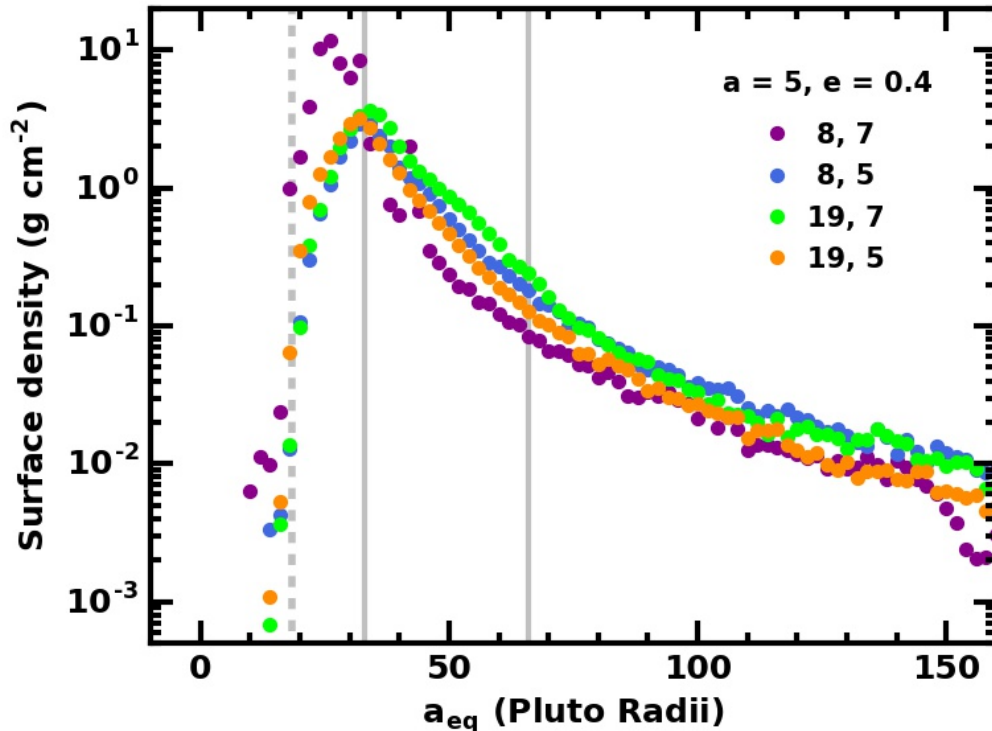


Figure 8. Surface density distributions for model 5–8 calculations with $M_0 = 10^{21}$ g. The legend indicates (a, e) for the central binary and (q_0, ι_0) for the solids in each calculation. The vertical grey lines show the boundaries of the satellite zone. The surface density rises from a sharp inner edge at $\sim 20 R_P$ to a sharp peak at $35 R_P$; the surface density then falls over two orders of magnitude from the peak to $150 R_P$. Ripples in the surface density at $80\text{--}150 R_P$ for the model with $(q_0, \iota_0) = (7, 0.25)$ are typical of disks that have not quite settled into an equilibrium state.

mass grows, the slope of the power-law drops; for $M_0 = 10^{23}$ g, $p \approx 2.5$. The shallower slope is a signature of the processes that generate the disk in the plane of the binary’s orbit. In more massive systems, the binary is more effective at placing material at larger distances, reducing the slope in $\Sigma(a)$ relative to systems with less initial mass.

Despite the sharp peaks in Σ , surviving solids beyond the satellite zone contain a large fraction of the final mass. In the most massive models with $M_0 = 10^{23}$ g, roughly equal amounts of mass lie within the satellite zone and at $a_{eq} \gtrsim 75 R_P$. In model 5, for example, the mass in the satellite zone is roughly 100 times the mass of the Pluto–Charon satellites. In the least massive models, the sharper drop in $\Sigma(a_{eq})$ leaves a smaller fraction of the final mass in solids beyond the satellite zone.

Outcomes of calculations with different combinations of (a, e) for the Pluto–Charon binary and q_0 for the solids lead to similar results. For each model and M_0 , Table 2 summarizes the mass remaining in active tracers at 1000 yr (M_f), the mass in disk material with $e \leq 0.1$ (M_d), the inner and outer edge of the disk (a_1, a_2), the location of peak surface density (a_m), and the maximum surface density (Σ_m). Disk edges are defined as the point where the surface density first rises above 10^{-2} g cm $^{-2}$ (inner edge) or where the surface density first drops below 10^{-2} g cm $^{-2}$ outside the peak surface density.

The Table collates several interesting features summarized in the discussions of models 3–8. The ratio of M_f and M_d to the initial mass M_0 declines with M_0 . Systems with a small initial mass, $M_0 = 10^{21}$ g, place

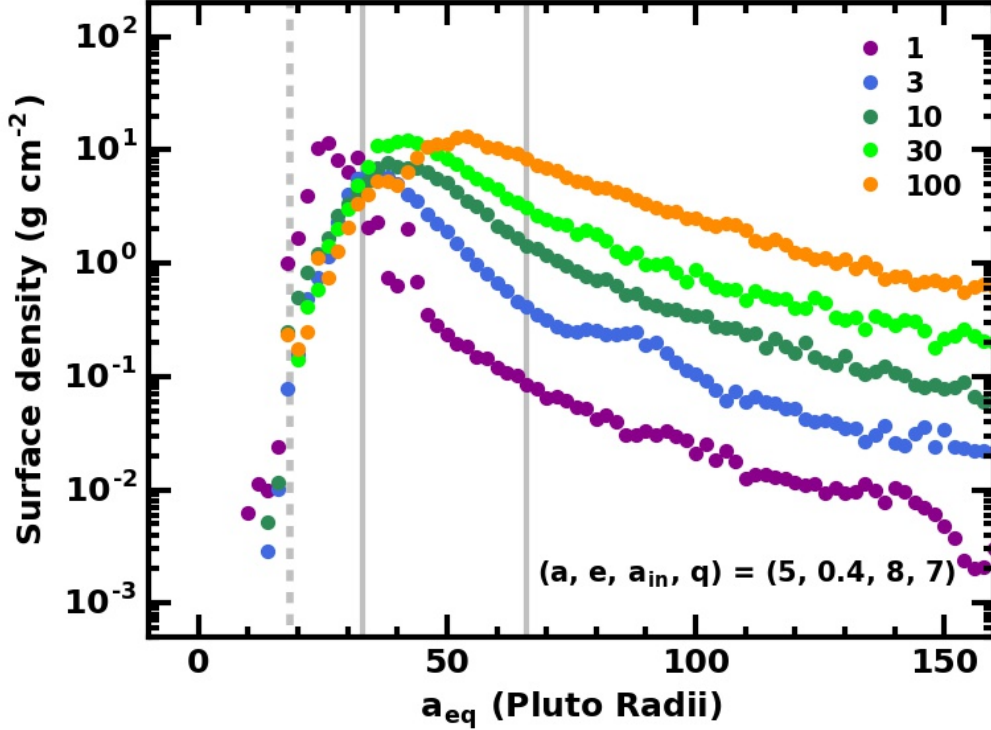


Figure 9. As in Fig. 8 for model 5 and various M_0 as indicated in the legend. Systems with larger initial mass have surface density maxima at larger semimajor axes.

10% to 30% of small solids into a disk. When the initial mass is 100 times larger, only $\sim 5\%$ of the initial mass remains in the system. In all cases, the inner edge of the disk is 3–4 times the separation of the inner binary, with $a_1 \approx 15\text{--}20 R_P$ when $a = 5 R_P$ and $a_1 \approx 35\text{--}45 R_P$ when $a \approx 10 R_P$. Peak surface density occurs at roughly twice a_1 . Although a_1 and a_m are independent of M_0 , the outer edge of the disk correlates well with M_0 , ranging from $a_2 \approx 125\text{--}150 R_P$ for $M_0 = 10^{21}$ g to $a_2 \approx 300\text{--}400 R_P$ for $M_0 = 10^{23}$ g. Systems with large disk radii have significant amount of solids outside the satellite zone.

To highlight one outcome from Table 2, Fig. 10 summarizes differences in the final surface density distributions with different central binaries. When the Pluto–Charon binary is compact and nearly circular, peak surface density is close to the inner edge of the satellite zone. As e grows, peak Σ moves outward. In Pluto–Charon binaries with $(a, e) = (5 R_P, 0.6)$, the surface density reaches a broad maximum at 50–60 Pluto–Charon, roughly coincident with the orbits of Kerberos and Hydra. For $e = 0.8$, the edge of the disk rests in the middle of the satellite zone; Σ has a sharp peak at ~ 85 Pluto–Charon, well outside the satellite zone.

In each calculation at $t = 1000$ yr, very little of the disk lies within regions where circumbinary orbits are unstable (e.g., Holman & Wiegert 1999; Doolin & Blundell 2011). In numerical simulations of circumbinary test particles, the innermost stable orbits for systems with mass ratios similar to Pluto–Charon lie at $14 R_P$ ($a, e = 5 R_P, 0.2$), $17\text{--}18 R_P$ ($a, e = 5 R_P, 0.4$), $38\text{--}42 R_P$ ($a, e = 10 R_P, 0.6$), and $46 R_P$ ($a, e = 10 R_P, 0.8$). Most of the results in Table 2 place the inner edge of the disk in the stable region of the system (see also Table 1). In the few examples where disk material lies within an unstable region, the binary will eject these solids within another few thousand years (Kenyon & Bromley 2019a).

Table 2. Disk Properties at 1000 yr^a

Model	M_0	M_f	M_d	a_1	a_2	a_m	Σ_m	Model	M_0	M_f	M_d	a_1	a_2	a_m	Σ_m
1	1	0.28	0.26	16	150	30	6.39	8	1	0.19	0.18	18	134	32	3.21
1	3	0.79	0.74	16	166	28	33.69	8	3	0.48	0.46	16	172	32	4.34
1	10	1.17	1.03	12	194	32	19.33	8	10	0.89	0.82	14	216	40	4.63
1	30	1.97	1.59	14	276	44	10.43	8	30	2.15	1.94	18	278	52	6.42
1	100	5.48	4.52	24	360	44	26.31	8	100	6.25	5.19	14	330	56	16.44
2	1	0.11	0.09	16	124	26	3.25	9	1	0.68	0.67	36	176	52	5.35
2	3	0.32	0.28	14	166	32	4.05	9	3	1.47	1.43	36	180	70	7.81
2	10	0.65	0.52	16	168	32	6.96	9	10	2.66	2.47	36	200	70	9.71
2	30	1.65	1.32	16	216	42	6.46	9	30	4.98	4.37	34	320	72	14.04
2	100	4.10	3.23	24	328	44	17.49	9	100	7.78	6.51	34	304	70	26.63
3	1	0.14	0.13	16	122	32	2.11	10	1	0.68	0.67	36	176	64	6.63
3	3	0.56	0.50	16	170	36	6.61	10	3	1.12	1.07	36	180	52	7.41
3	10	1.17	1.00	16	196	38	7.72	10	10	2.08	1.91	34	202	52	9.78
3	30	2.49	1.86	20	266	42	12.18	10	30	4.40	3.85	34	272	72	13.39
3	100	4.76	3.61	18	384	54	13.14	10	100	7.74	6.52	42	394	94	18.45
4	1	0.22	0.20	18	158	32	2.96	11	1	0.58	0.58	38	166	60	6.38
4	3	0.43	0.38	16	174	36	3.41	11	3	1.65	1.60	36	184	70	9.50
4	10	1.01	0.86	18	206	40	6.41	11	10	2.92	2.75	36	212	70	11.11
4	30	2.19	1.82	18	238	33	10.43	11	30	4.07	3.59	36	268	72	11.87
4	100	4.60	3.66	16	316	54	12.10	11	100	7.79	6.73	36	404	80	15.16
5	1	0.35	0.33	18	154	32	5.16	12	1	0.12	0.12	36	150	54	2.09
5	3	0.57	0.52	18	168	36	6.12	12	3	0.50	0.47	34	170	60	5.86
5	10	1.13	0.98	18	200	40	8.29	12	10	1.93	1.80	36	200	52	8.89
5	30	2.26	1.88	18	296	44	10.69	12	30	4.05	3.62	34	260	72	11.05
5	100	4.34	3.37	18	310	52	11.18	12	100	7.26	6.28	36	370	78	16.25
6	1	0.26	0.22	18	148	34	4.00	13	1	0.78	0.78	48	168	86	7.60
6	3	0.39	0.34	18	168	34	3.74	13	3	1.88	1.85	46	182	92	13.80
6	10	1.14	0.99	18	176	40	9.54	13	10	4.07	3.90	40	198	92	25.00
6	30	2.25	1.87	20	274	44	12.69	13	30	5.53	5.00	38	266	94	19.78
6	100	4.11	3.08	18	342	54	9.45	13	100	7.55	5.73	44	378	94	15.72
7	1	0.26	0.24	18	158	34	3.69	14	1	0.12	0.11	48	110	52	2.24
7	3	0.42	0.40	16	170	36	3.18	14	3	0.55	0.52	48	168	88	4.28
7	10	1.15	1.05	14	188	46	5.71	14	10	2.55	2.45	46	192	94	17.64
7	30	1.86	1.67	14	238	40	7.39	14	30	4.40	3.85	42	232	94	13.09
7	100	4.65	4.02	16	312	46	15.35	14	100	7.74	6.52	42	394	94	18.45

^a For each model number, the columns list the initial mass in solids M_0 , the final mass in solids M_f , and the final mass in the disk, M_d , in units of 10^{21} g; the inner and outer disk radius, a_1 and a_2 (in units of R_P); the radius of maximum surface density, a_m , in R_P , and the maximum surface density Σ_m in units of g cm^{-2} .

Although the binary clearly sets the inner edge of the disk, collisional damping and the gravitational potential of the binary combine with the initial conditions to establish the overall disk morphology. In compact binaries with $a = 5 R_P$, some circumbinary solids initially have orbits with semimajor axes that are stable for particles on circular orbits. Others have semimajor axes within the unstable zone. As collisional damping circularizes the solids, the binary potential encourages them to move onto orbits with larger a . Over 1000 yr, the binary evacuates the volume where orbits are unstable, leaving behind solids on stable orbits. Because solids were nearly on stable orbits at $t = 0$, the final orbits for many solids lie close to the inner edge of the stable region.

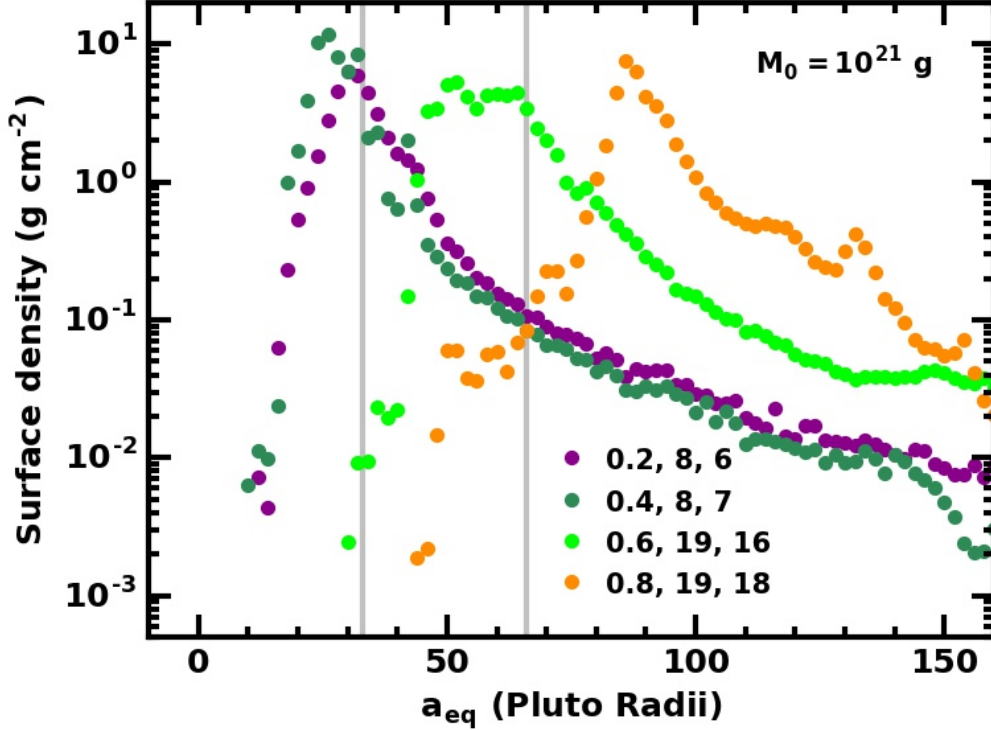


Figure 10. Comparison of surface density distributions at 1000 yr for calculations with $M_0 = 10^{21}$ g and the combinations of e , a_{in} , and q_0 indicated in the legend. The vertical grey lines indicate the boundaries of the satellite zone. In compact Pluto–Charon binaries with $a = 5 R_P$ and $e = 0.2$ – 0.4 , the surface density reaches a maximum at the inner edge of the satellite zone, ~ 30 – $35 R_P$. In wider binaries with $a = 10 R_P$ and $e = 0.6$ – 0.8 , peak surface density lies at larger a_{eq} , 50 – $60 R_P$ when $e = 0.6$ and 80 – $90 R_P$ when $e = 0.8$. Systems with $e = 0.8$ have peak Σ outside the satellite zone.

In contrast, solids orbiting less compact, more eccentric binaries all initially lie within the unstable region. Although collisional damping has a somewhat bigger challenge in circularizing the orbits of these solids, wider binaries with longer orbital periods push on the solids more gently. As the solids move farther and farther away from the binary, damping has time to circularize the orbits. Because the unstable region around the binary is large, solids have to find stable orbits well outside the binary.

In these examples, particles on circular orbits at the inner edge of the satellite zone are stable (unstable) in binaries with $a = 5 R_P$ and $e = 0.2$ – 0.4 ($a = 10 R_P$ and $e = 0.6$ – 0.8). This difference results in very different disk morphologies: circumbinary disks in compact binaries have significant mass within the satellite zone; disks in wider binaries have most of their mass outside the satellite zone.

To conclude this section, Fig. 11 compares results for Σ from model 5 (green symbols, $M_0 = 10^{21}$ g) and model 11 (orange symbols, $M_0 = 10^{21}$ g) with the surface density distribution for debris from the impact of a TNO with Charon (purple symbols; Bromley & Kenyon 2020). In the TNO collision, 60% to 70% of the 10^{20} g ejected by the impact survives to form a circumbinary ring. Although this ring contains less material than required to build the known circumbinary satellites, the surface density maximum coincides with the maximum of disks surrounding a Pluto–Charon binary with $e = 0.6$. The inner edge of this ring also roughly overlays the inner edge of the disk around the more eccentric binary.

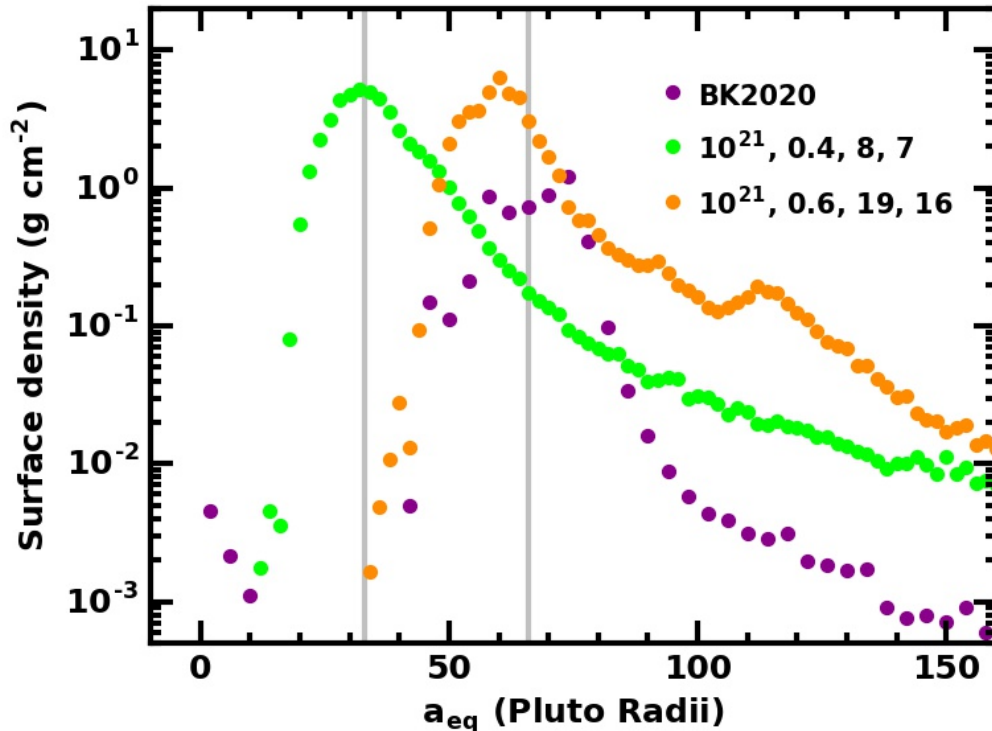


Figure 11. Comparison of surface density distributions generated from the impact of a TNO on Charon (BK2020, purple symbols Bromley & Kenyon 2020) with the final states of debris surrounding the giant impact that forms the Pluto–Charon binary. Green (orange) symbols indicate results for $M_0, e, a_{in}, q_0 = 10^{21} \text{ g}, 0.4, 8 R_P, 7 R_P$ ($10^{21} \text{ g}, 0.6, 19 R_P, 16 R_P$). The vertical grey lines indicate the boundaries of the satellite zone.

The sharp outer edge of rings produced from TNO collisions with Charon provides a sharp contrast with the disks generated from giant impacts. From the peak at $80 R_P$ to $100 R_P$, the surface density within the ring drops by nearly three orders of magnitude. Within disks from the giant impact, the decline in Σ is a more modest factor of ten. The gradual decline in Σ is a hallmark of all of the extended disks in our calculations.

4. DISCUSSION

Over the past decade, the giant impact hypothesis has become the most popular model for the formation of the Pluto–Charon binary planet (e.g., McKinnon et al. 2017; Stern et al. 2018; McKinnon et al. 2020, and references therein). In the commonly accepted picture, two planets orbiting the Sun within the protosolar nebula suffer a glancing collision (Canup 2005, 2011). The lower mass secondary loses momentum and is captured by the more massive primary; debris from the collision orbits the newly-formed, compact binary. In a more recent option, the planets first form a very wide binary (Rozner et al. 2020). Over time, the orbit decays, which facilitates a collision with a geometry similar to that in a giant impact.

Immediately after the collision, the circumbinary debris lies on very eccentric orbits that are intrinsically unstable. Within this debris, solid particles follow one of two dynamical paths (Kenyon & Bromley 2014b; Walsh & Levison 2015; Kenyon & Bromley 2019c; Bromley & Kenyon 2020). Solids that do not physically

collide with other solids cannot circularize their orbits. Within a month, the binary either ejects these solids or accretes them. When an orbiting solid collides with another solid, the large relative collision velocities guarantee catastrophic disruption; particles within the debris are then much smaller than the original solids. After only a few such collisions, 1–10 km solids can be ground down into 1–10 m solids (Kenyon & Bromley 2014b; Bromley & Kenyon 2020). Because small solids damp effectively, this process allows solids to circularize their orbits on short time scales.

In a first attempt to chart the evolution of solids following the giant impact, Walsh & Levison (2015) performed a set of numerical calculations of high eccentricity particles with initial semimajor axes between the 3:1 and 5:1 orbital resonances with Charon¹. Although some solids eventually cross Charon’s orbit and are ejected from the binary, initial orbits have pericenters well outside the apocenter of Charon’s orbit. Within this suite of calculations, systems with sufficiently large numbers of inter-particle collisions per orbit develop circumbinary disks with relatively few losses from dynamical ejections. The combination of collisional damping and dynamical interactions with Charon generate extended disks on stable circumbinary orbits. For binaries with $e = 0.0$ – 0.3 , disk material orbits outside the 4:1 orbital resonance with Charon and inside the 7:1 resonance. Disks orbiting more eccentric binaries are more extended than those orbiting more circular binaries. With little loss in mass from dynamical ejections, all disks have enough mass in the satellite zone to grow several 10–20 km moons. The lack of mass outside the orbit of Hydra eliminates the possibility of satellite growth outside the satellite zone.

The calculations described here complement and extend these results. In models 1–14, the solids begin on eccentric orbits that cross Charon’s orbit (models 2, 4, 6, 8, 10, 12, and 14) or have pericenters at the apocenter of Charon’s orbit (models 1, 3, 5, 7, 9, 11, and 13). Compared to Walsh & Levison (2015), the central binary has a broader range of eccentricity, $e = 0.2$ – 0.8 instead of $e = 0.0$ – 0.3 . The range of initial solid mass considered here is also somewhat larger than in Walsh & Levison (2015).

Despite differences in initial conditions, outcomes are similar. In all of the 70 calculations discussed here, the binary ejects a substantial fraction of solids from the system. Compared to Walsh & Levison (2015), the initial orbital states of the solids are much more extreme; thus, collisional damping is unable to circularize the orbit of every solid in the system. Despite the ejections, disk formation is ubiquitous. The inner structure of the disk is fairly similar to results described in Walsh & Levison (2015), with an inner edge just outside the region where circumbinary orbits are unstable and a maximum Σ at somewhat larger radii.

However, the disks considered here are much more extensive than those in Walsh & Levison (2015), with outer radii of 150–400 R_P . The initial conditions are responsible for this difference. By starting on orbits that cross or nearly cross the orbit of Charon, the solids considered here receive much larger kicks from the central binary and are pushed much farther away from the system barycenter. Collisional damping still effectively circularizes orbits, but generates much larger disks. Within these disks, the mass in solids ranges from ~ 1 to 50–70 times the mass in the known Pluto–Charon satellites.

Although every disk has mass sufficient to form moons like the current Pluto–Charon satellites, all disks may not generate satellites in their current locations. In systems where Pluto–Charon has an initial $e = 0.2$ – 0.4 , the surface density peak lies at the inner edge of the satellite zone (Fig. 10). These disks have a factor of 5–6 less mass near the orbit of Hydra than near the orbits of Styx and Nix. In contrast, disks orbiting Pluto–Charon binaries with $e = 0.6$ have most of their mass near the orbits of Kerberos and Hydra

¹ For a binary semimajor axis $a = 10 R_P$, the 3:1, 5:1, and 7:1 resonances have semimajor axes of $\sim 20 R_P$, $30 R_P$, and $36 R_P$.

and relatively little near Styx–Nix. Finally, systems with an initial $e = 0.8$ form disks with nearly all of their mass outside the satellite zone at $a \gtrsim 80 R_P$.

Clearly, understanding which disks form satellites with masses and orbital architectures similar to the Pluto–Charon satellites requires a more extensive set of calculations. However, results in [Kenyon & Bromley \(2014b\)](#) and [Walsh & Levison \(2015\)](#) provide useful guidance. Among the systems considered here, those with $e \approx 0.4$ – 0.6 seem most likely to generate large moons in the satellite zone. In binaries with $e = 0.2$ (0.8), newly-formed moons would need to migrate outward (inward) to reach the same locations as the known satellites. For all binaries, disks have a fraction of their mass outside the satellite zone. Formation of massive satellites in this region is plausible ([Kenyon & Bromley 2014b](#)). If these disks form satellites, the moons must either be small enough to avoid detection by *New Horizons* ([Weaver et al. 2016](#)) or migrate from large distances into the satellite zone ([Kenyon & Bromley 2014b](#)).

For any circumbinary disk in the Pluto–Charon system, several evolutionary processes impact satellites as they grow within the disk. Right after the giant impact, tidal forces begin to circularize and then to expand the Pluto–Charon orbit (e.g., [Farinella et al. 1979](#); [Dobrovolskis et al. 1997](#); [Peale 1999](#); [Cheng et al. 2014a](#); [Correia 2020](#)). If satellites grow rapidly as in [Walsh & Levison \(2015\)](#), orbital resonances sweep through the satellite zone ([Ward & Canup 2006](#); [Lithwick & Wu 2008](#); [Cheng et al. 2014b](#)). Satellite orbits are then rapidly destabilized. More slowly growing satellites as in [Kenyon & Bromley \(2014b\)](#) may retain sufficient mass in small particles to stabilize the orbits of large moons ([Kenyon & Bromley 2014b](#); [Bromley & Kenyon 2015b](#)). Dynamical calculations of massless tracer particles suggest a ~ 0.1 – 10 Myr time scale to remove small particles orbiting between the four satellites ([Kenyon & Bromley 2014b, 2019a](#)). Because tides expand the orbit on a similar time scale, it is important to include tidal expansion in calculations of particle growth. We plan to complete these types of calculations in the near future.

Aside from tidal evolution of the central binary, gravitational interactions with the Sun can influence the formation and evolution of moons in the Pluto–Charon binary ([Michaely et al. 2017](#)). Recent analyses suggest the Sun truncates any circumbinary Pluto–Charon disk at 400 – $500 R_P$. Although gravity of the Sun does not affect solids within the satellite zone, Lidov–Kozai oscillations can place particles in the outer disk on high e orbits. These particles might then collide with solids in the inner disk, adding their mass to the satellite zone and enhancing the formation of large moons. We have not included the Sun in the calculations discussed here, but it is straightforward to do so. Adding the Sun might reduce the extent of the circumbinary disks and enable the formation of more massive satellites in the inner disk.

Despite the popularity of the giant impact picture for satellite formation in Pluto–Charon, it is plausible that satellites form in the debris from an impact between Charon and a TNO ([Bromley & Kenyon 2020](#)). Because debris from such a collision naturally forms a circumbinary ring, this model is attractive. Satellites form only near or within the satellite zone, with a much smaller chance of moon formation outside the satellite zone. If the TNO collision occurs after the completion of tidal evolution, newly-formed satellites need not dodge expanding orbital resonances from the binary. The circumbinary rings of [Bromley & Kenyon \(2020\)](#) are also safe from Lidov–Kozai oscillations.

Choosing among possible models requires calculations that include the physical processes outlined above. It seems plausible that at least one configuration of a circumbinary disk or ring will yield satellites similar to the known satellites. Aside from explaining the origin of the satellites, these calculations may constrain the properties of the giant impact (by establishing a preference for a small range of initial binary a and e) or the space density of TNOs after Pluto–Charon reaches its current tidally locked state.

5. SUMMARY

We consider the dynamical evolution of circumbinary solids following the giant impact that formed Pluto–Charon. Starting from initial orbits that cross or nearly cross Charon’s orbit, particles respond to the time-varying binary potential and damping from particle–particle collisions. On time scales of 100–1000 yr, the central binary ejects a large fraction of the solids into the Solar System. At the same time, collisional damping circularizes the orbits of many other particles. The combined action of damping and gravitational pushes from Pluto–Charon yields a vertically thin circumbinary disk (see also [Walsh & Levison 2015](#)). The disk extends from close to the innermost stable circumbinary orbit at 20–40 R_P to 200–400 R_P . Within the disk, the maximum surface density is often within the ‘satellite zone,’ the circumbinary volume that contains the orbits of the four small satellites orbiting Pluto–Charon.

Although all initial conditions lead to disk formation, outcomes depend on the properties of the Pluto–Charon binary and the initial orbital architecture of the circumbinary debris from the giant impact. Wider binaries with $a = 10 R_P$ and $e = 0.6–0.8$ retain a larger fraction of the impact debris than more compact binaries with $a = 5 R_P$ and $e = 0.2–0.4$. Debris fields with less mass, $\sim 10^{21}$ g, and a smaller fraction of orbits with pericenters inside Charon’s orbit preserve more of their initial mass than those with more mass and Charon-crossing orbits. Despite these differences, all calculations retain enough mass to form several 5–20 km satellites. However, some configurations may enable the growth of large satellites well outside the orbit of Hydra, which is precluded by *New Horizons* imaging data.

With the calculations of [Bromley & Kenyon \(2020\)](#), there are now two plausible paths for the formation of the Pluto–Charon circumbinary satellites. In the giant impact model, the conditions within circumbinary disks are favorable for growing small moons in less than 1 Myr. As these moons form, they must survive tidal expansion of the central binary. In a small impact model, debris from the collision between Charon and a TNO evolves into a circumbinary ring of material roughly coincident with the satellite zone. As the binary has already evolved into its current configuration, satellites generated within this ring need not worry about tidal expansion.

Choosing between these two scenarios requires additional calculations that include tidal evolution and interaction with the Sun and allow for orbital migration of the satellites. If a robust choice is possible, these calculations could provide additional constraints on the formation of Pluto–Charon by isolating a range of initial a and e that is more conducive to the growth and survival of Styx, Nix, Kerberos, and Hydra. Outcomes of impacts between Charon and large TNOs could yield better estimates of the cratering frequency on Pluto–Charon and the early evolution of large solids in the Kuiper belt (e.g., [Singer et al. 2019](#); [Kenyon & Bromley 2020](#)).

Some of the data (ascii or binary output files and C programs capable of reading them) generated from previous numerical studies of the Pluto–Charon system are available at a publicly-accessible repository (<https://hive.utah.edu/>) with these urls <https://doi.org/10.7278/s50d-w273-1gg0> ([Kenyon & Bromley 2019a](#)), <https://doi.org/10.7278/S50D-HAJT-E0G0> ([Kenyon & Bromley 2019b](#)), <https://doi.org/10.7278/S50D-EFCY-ZC00> ([Kenyon & Bromley 2019c](#)), <https://doi.org/10.7278/S50D4AKFQZFC> ([Bromley & Kenyon 2020](#)), and <https://doi.org/10.7278/S50D5Q2MFDBT> ([Kenyon & Bromley 2020](#)). For this paper, data are available at the same repository, with the url <https://doi.org/10.7278/S50DSSMBHXXN>.

We acknowledge generous allotments of computer time on the NASA ‘discover’ cluster. Advice and comments from M. Geller and an anonymous referee improved the presentation of these results. Portions of this project were supported by the NASA *Outer Planets* and *Emerging Worlds* programs through grants NNX11AM37G and NNX17AE24G.

REFERENCES

- Agnor, C., & Asphaug, E. 2004, *ApJL*, 613, L157
 Agnor, C. B., Canup, R. M., & Levison, H. F. 1999, *Icarus*, 142, 219
 Andersson, L. E., & Fix, J. D. 1973, *Icarus*, 20, 279
 Asphaug, E. 2014, *Annual Review of Earth and Planetary Sciences*, 42, 551
 Asphaug, E., Agnor, C. B., & Williams, Q. 2006, *Nature*, 439, 155
 Bromley, B. C., & Kenyon, S. J. 2006, *AJ*, 131, 2737
 —. 2011a, *ApJ*, 731, 101
 —. 2011b, *ApJ*, 735, 29
 —. 2013, *ApJ*, 764, 192
 —. 2015a, *ApJ*, 806, 98
 —. 2015b, *ApJ*, 809, 88
 —. 2020, arXiv e-prints, arXiv:2006.13901
 —. 2021, *AJ*, 161, 25
 Brozović, M., Showalter, M. R., Jacobson, R. A., & Buie, M. W. 2015, *Icarus*, 246, 317
 Buie, M. W., Grundy, W. M., & Tholen, D. J. 2013, *AJ*, 146, 152
 Buie, M. W., Grundy, W. M., Young, E. F., Young, L. A., & Stern, S. A. 2010a, *AJ*, 139, 1117
 —. 2010b, *AJ*, 139, 1128
 Buie, M. W., Tholen, D. J., & Grundy, W. M. 2012, *AJ*, 144, 15
 Canup, R. M. 2004, *ARA&A*, 42, 441
 —. 2005, *Science*, 307, 546
 —. 2011, *AJ*, 141, 35
 Canup, R. M., & Asphaug, E. 2001, *Nature*, 412, 708
 Cheng, W. H., Lee, M. H., & Peale, S. J. 2014a, *Icarus*, 233, 242
 Cheng, W. H., Peale, S. J., & Lee, M. H. 2014b, *Icarus*, 241, 180
 Christy, J. W., & Harrington, R. S. 1978, *AJ*, 83, 1005
 Correia, A. C. M. 2020, *A&A*, 644, A94
 Dobrovolskis, A. R., Peale, S. J., & Harris, A. W. 1997, in *Pluto and Charon*, ed. S. A. Stern & D. J. Tholen (Tucson: University of Arizona Press), 159
 Doolin, S., & Blundell, K. M. 2011, *MNRAS*, 418, 2656
 Durda, D. D. 1996, *Icarus*, 120, 212
 Durda, D. D., & Dermott, S. F. 1997, *Icarus*, 130, 140
 Farinella, P., Milani, A., Nobili, A. M., & Valsecchi, G. B. 1979, *Moon and Planets*, 20, 415
 Genda, H., Fujita, T., Kobayashi, H., Tanaka, H., & Abe, Y. 2015a, *Icarus*, 262, 58
 Genda, H., Kobayashi, H., & Kokubo, E. 2015b, *ApJ*, 810, 136
 Genda, H., Kokubo, E., & Ida, S. 2012, *ApJ*, 744, 137
 Giuliani Winter, S. M., Winter, O. C., Vieira Neto, E., & Sfair, R. 2013, *MNRAS*, 430, 1892
 —. 2014, *MNRAS*, 439, 3300
 —. 2015, *Icarus*, 246, 339
 Goldreich, P., Lithwick, Y., & Sari, R. 2004, *ARA&A*, 42, 549
 Greenberg, R., Hartmann, W. K., Chapman, C. R., & Wacker, J. F. 1978, *Icarus*, 35, 1
 Grundy, W. M., Binzel, R. P., Buratti, B. J., et al. 2016, *Science*, 351, aad9189
 Holman, M. J., & Wiegert, P. A. 1999, *AJ*, 117, 621
 Ida, S., Canup, R. M., & Stewart, G. R. 1997, *Nature*, 389, 353
 Kenyon, S. J. 2002, *PASP*, 114, 265
 Kenyon, S. J., & Bromley, B. C. 2002, *AJ*, 123, 1757
 —. 2004, *AJ*, 127, 513
 —. 2006, *AJ*, 131, 1837
 —. 2008, *ApJS*, 179, 451
 —. 2014a, *ApJ*, 780, 4
 —. 2014b, *AJ*, 147, 8
 —. 2016, *ApJ*, 817, 51
 —. 2019a, *AJ*, 157, 79
 —. 2019b, *AJ*, 158, 69
 —. 2019c, *AJ*, 158, 142
 —. 2020, *The Planetary Science Journal*, 1, 40
 Kenyon, S. J., Najita, J. R., & Bromley, B. C. 2016, *ApJ*, 831, 8
 Lee, M. H., & Peale, S. J. 2006, *Icarus*, 184, 573
 Leinhardt, Z. M., Richardson, D. C., & Quinn, T. 2000, *Icarus*, 146, 133
 Leinhardt, Z. M., & Stewart, S. T. 2009, *Icarus*, 199, 542
 Leung, G. C. K., & Lee, M. H. 2013, *ApJ*, 763, 107
 Lissauer, J. J. 1987, *Icarus*, 69, 249

- Lithwick, Y., & Wu, Y. 2008, ArXiv e-prints, arXiv:0802.2939
- Lock, S. J., Stewart, S. T., Petaev, M. I., et al. 2018, *Journal of Geophysical Research (Planets)*, 123, 910
- McKinnon, W. B., Glein, C. R., Bertrand, T., & Rhoden, A. R. 2020, arXiv e-prints, arXiv:2011.14030
- McKinnon, W. B., Nimmo, F., Wong, T., et al. 2016, *Nature*, 534, 82
- McKinnon, W. B., Stern, S. A., Weaver, H. A., et al. 2017, *Icarus*, 287, 2
- Michaely, E., Perets, H. B., & Grishin, E. 2017, *ApJ*, 836, 27
- Nakajima, M., & Stevenson, D. J. 2014, *Icarus*, 233, 259
- . 2018, *Earth and Planetary Science Letters*, 487, 117
- Nimmo, F., Umurhan, O., Lisse, C. M., et al. 2017, *Icarus*, 287, 12
- Ohtsuki, K. 1992, *Icarus*, 98, 20
- Ohtsuki, K., Stewart, G. R., & Ida, S. 2002, *Icarus*, 155, 436
- Pahlevan, K., Karato, S.-i., & Fegley, B. 2016, *Earth and Planetary Science Letters*, 445, 104
- Peale, S. J. 1999, *ARA&A*, 37, 533
- Quintana, E. V., Barclay, T., Borucki, W. J., Rowe, J. F., & Chambers, J. E. 2016, *ApJ*, 821, 126
- Rozner, M., Grishin, E., & Perets, H. B. 2020, *MNRAS*, 497, 5264
- Showalter, M. R., & Hamilton, D. P. 2015, *Nature*, 522, 45
- Showalter, M. R., Hamilton, D. P., Stern, S. A., et al. 2011, *IAUC*, 9221, 1
- Showalter, M. R., Weaver, H. A., Stern, S. A., et al. 2012, *IAUC*, 9253, 1
- Singer, K. N., Grundy, W. M., White, O. L., & Binzel, R. P. 2021, *Icarus*, 356, 114269
- Singer, K. N., McKinnon, W. B., Gladman, B., et al. 2019, *Science*, 363, 955
- Stern, S. A., Grundy, W. M., McKinnon, W. B., Weaver, H. A., & Young, L. A. 2018, *ARA&A*, 56, 357
- Stern, S. A., Bagenal, F., Ennico, K., et al. 2015, *Science*, 350, aad1815
- Stewart, S. T., & Leinhardt, Z. M. 2012, *ApJ*, 751, 32
- Tang, H., & Young, E. D. 2020, *The Planetary Science Journal*, 1, 49
- Walsh, K. J., & Levison, H. F. 2015, *AJ*, 150, 11
- Ward, W. R., & Canup, R. M. 2006, *Science*, 313, 1107
- Weaver, H. A., Buie, M. W., Buratti, B. J., et al. 2016, *Science*, 351, aae0030
- Weidenschilling, S. J., Spaute, D., Davis, D. R., Marzari, F., & Ohtsuki, K. 1997, *Icarus*, 128, 429
- Wetherill, G. W. 1980, *ARA&A*, 18, 77
- Winter, S. M. G., Winter, O. C., Guimarães, A. H. F., & Silva, M. R. 2010, *MNRAS*, 404, 442
- Woo, J. M. Y., & Lee, M. H. 2018, *AJ*, 155, 175
- Youdin, A. N., Kratter, K. M., & Kenyon, S. J. 2012, *ApJ*, 755, 17